HHS Public Access

Author manuscript

Cell. Author manuscript; available in PMC 2021 August 06.

Published in final edited form as:

Cell. 2020 August 06; 182(3): 545–562.e23. doi:10.1016/j.cell.2020.06.030.

Type V collagen in scar tissue regulates the size of scar after heart injury

Tomohiro Yokota[1,2,3,4,5,6], **Jackie McCourt**[7], **Feiyang Ma**[3,4,5], **Shuxun Ren**[5,8], **Shen Li**[1,2,3,4,5,6], **Tae-hyung Kim**[7], **Yerbol. Z Kurmangaliyev**[9], **Rohollah Nasiri**[6,10,11], **Samad Ahadian**[6,10,12], **Thang Nguyen**[10], **Marvin Haw**[6,10,15], **Yonggang Zhou**[1,2,3,4,5,6], **Rimao Wu**[1,2,3,4,5,6], **Abraham Rodriguez**[1,2,3,4,5,6], **Whitaker Cohn**[16], **Yibin Wang**[5,8], **Julian Whitelegge**[16], **Sergey Ryazantsev**[6], **Ali Khademhosseini**[6,10,12,13,14], **Michael A. Teitell**[10,18], **Eric Chiou**[6,10,15], **David E. Birk**[19], **Amy C. Rowat**[7,10], **Rachelle H. Crosbie**[4,5,7], **Matteo Pellegrini**[3,4,5], **Marcus Seldin**[17], **Aldons J. Lusis**[1,20], **Arjun Deb**[*,**,1,2,3,4,5,6]

[1]Division of Cardiology, Department of Medicine, David Geffen School of Medicine, University of California, Los Angeles, CA 90095

[2]UCLA Cardiovascular theme, David Geffen School of Medicine, University of California, Los Angeles, CA 90095

[3]Department of Molecular, Cell and Developmental Biology, College of Letters and Sciences, University of California, Los Angeles, CA 90095

[4]Eli & Edythe Broad Center of Regenerative Medicine and Stem Cell Research, University of California, Los Angeles, CA 90095

[5]Molecular Biology Institute, University of California, Los Angeles, CA 90095

[6]California Nanosystems Institute, University of California, Los Angeles, CA 90095

[7]Department of Integrative Biology and Physiology, University of California, CA 90095

[8]Department of Anesthesiology, David Geffen School of Medicine, University of California, Los Angeles, CA 90095

[**]Correspondence: Arjun Deb, MD, McDonald Research Laboratories 3609A, 675 Charles E Young Drive S, University of California, Los Angeles, CA 90095, adeb@mednet.ucla.edu, Phone: 310-825-9911.

Author Contributions

TY performed majority of experiments and analyzed data including cardiac imaging. SL, YZ, RW, and AR assisted in bench experiments. SR and YW performed animal surgeries, YK, FM, and MP analyzed RNA-seq and sc RNA-seq, JLM and RHC performed, analyzed, and interpreted AFM experiments, TN and MT performed and analyzed QPM experiments, T-HK and ACR performed and interpreted PMF experiments, MH and EC performed and interpreted traction force microscopy experiments, RN, SA, and AK performed and analyzed contraction of tissue scaffolds, WC and JW performed mass spectroscopy experiments, MS and AJL analyzed HMDP data, SR performed TEM, DEB provided key reagents and contributed towards discussion, AD conceptualized the project, supervised data collection and analysis and wrote the manuscript.

[*]Lead Contact: Further information and requests for resources and reagents should be directed to and will be fulfilled by Arjun Deb (adeb@mednet.ucla.edu)

Declaration of Interests

The authors declare no competing interests. Based on this work, patent No: 63/002,828 “Compositions and methods for treating dysregulated wound healing” has been filed and assigned to the Regents of the University of California.

[9]Department of Biological Chemistry, David Geffen School of Medicine, Los Angeles, CA 90095

[10]Department of Bioengineering, School of Engineering, University of California, Los Angeles, CA 90095

[11]Department of Mechanical Engineering, Sharif University of Technology, Tehran 11365-11155, Iran

[12]Terasaki Institute for Biomedical Innovation (TIBI), Los Angeles, CA 90024, USA

[13]Department of Chemical Engineering, School of Engineering, University of California, Los Angeles, CA 90095

[14]Department of Radiology, David Geffen School of Medicine, University of California, Los Angeles, CA 90095

[15]Department of Mechanical and Aerospace Engineering, University of California, Los Angeles, CA 90095

[16]Passarow Mass Spectrometry Laboratory, Semel Institute for Neuroscience and Behaviour, David Geffen School of Medicine, Los Angeles, CA 90095

[17]Department of Biological Chemistry and Center for Epigenetics and Metabolism, University of California, Irvine, CA 92697

[18]Department of Pathology and Laboratory Medicine, University of California, Los Angeles, CA 90095

[19]University of South Florida College of Medicine, Tampa, FL 33612

[20]Department of Genetics, David Geffen School of Medicine, Los Angeles, CA 90095

Summary

Scar tissue size following myocardial infarction is an independent predictor of cardiovascular outcomes, yet little is known about factors regulating scar size. We demonstrate that collagen V, a minor constituent of heart scars regulates the size of heart scars after ischemic injury. Depletion of collagen V led to a paradoxical increase in post infarction scar size with worsening of heart function. A systems genetics approach across 100 in-bred strains of mice demonstrated that collagen V is a critical driver of postinjury heart function. We show that collagen V deficiency alters the mechanical properties of scar tissue and altered reciprocal feedback between matrix and cells induce expression of mechanosensitive integrins that drive fibroblast activation and increase scar size. Cilengitide, an inhibitor of specific integrins, rescues the phenotype of increased post injury scarring in collagen V deficient mice. These observations demonstrate that collagen V regulates scar size in an integrin dependent manner.

Graphical Abstract

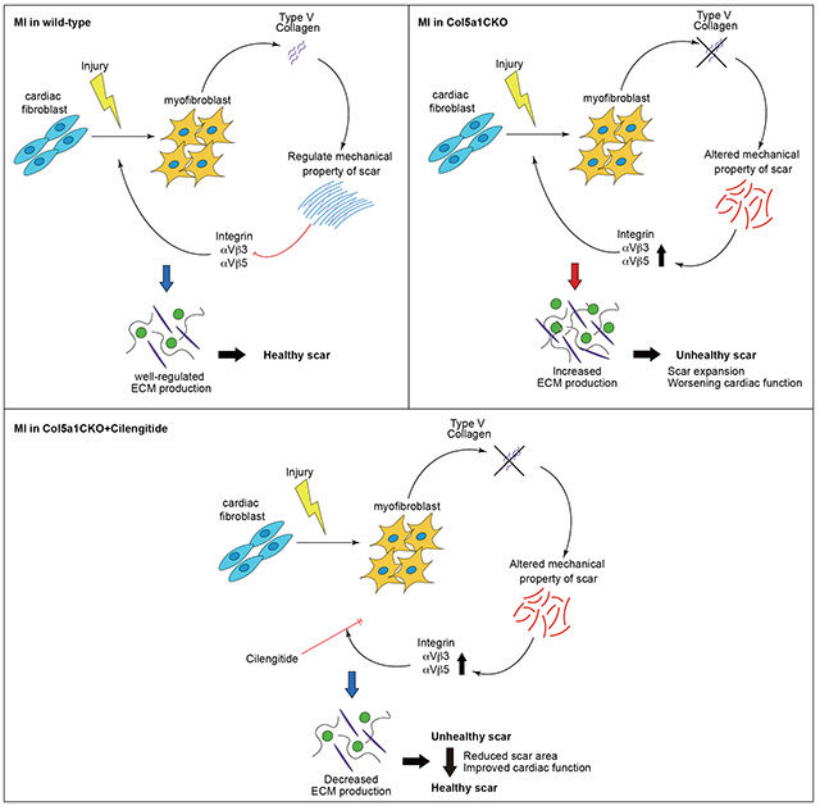

In Brief

Scar tissue size following heart injury is a predictor of cardiovascular outcomes. Yokota et al, find that a specific collagen, type V, plays a paradoxical role in limiting scar size by altering the mechanical properties of developing scar tissue.

Introduction

Following acute myocardial infarction, dead cardiac muscle is replaced by scar tissue. Clinical studies demonstrate that scar size in patients with prior myocardial infarction is an independent predictor of mortality and outcomes, even when normalized with respect to cardiac function(Gulati et al., 2013). Despite the immense pathophysiologic importance of scar burden, little is known about factors that regulate scar size after ischemic cardiac injury(Frangogiannis, 2017).

To identify factors determining scar size after myocardial infarction, we subjected animals to ischemic cardiac injury and performed transcriptional profiling of heart scars isolated from 3 days to 6 weeks post injury. We observed that scars rapidly attained transcriptional maturity and there were minimal transcriptional changes in the maturing scar tissue beyond 2 weeks of injury. We thus hypothesized that genes that regulate scar size are likely to be differentially expressed early after ischemic injury. Collagens were one of the most highly differentially upregulated genes in the injured heart early after ischemic cardiac injury. Collagens I and III are the most abundant collagens present in the uninjured heart

comprising approximately 90-95% of all cardiac collagens (Bashey et al., 1992; Frangogiannis, 2017; Weber, 1989). They belong to the family of fibrillar collagens that are thought to confer mechanical strength to the cardiac matrix. However, more than 26 different types of collagens have been described in mammals and we observed a large number of collagens, that are minimally expressed in the uninjured heart to be robustly induced following injury. The physiological necessity for the heterogeneity of collagen expression in scar tissue is unclear.

In this report, we demonstrate that collagen V, a fibrillar collagen that is minimally expressed in the uninjured heart and a minor component of scar tissue limits scar size after ischemic cardiac injury. Animals lacking Col V in scar tissue exhibit a significant and paradoxical increase in scar size after ischemic injury. In the absence of Col V, scars exhibit altered mechanical properties that drive integrin dependent mechanosensitive feedback on fibroblasts augmenting fibroblast activation, ECM secretion and increase in scar size. Modulation of such mechanosensitive feedback cues rescues the Col V deficient phenotype of increased scarring. These findings provide insight into the physiological role of Col V in regulating scar size and have implications for the treatment of dysregulated wound healing in genetic diseases caused by mutations in Col V encoding genes.

Results

Heart scars attain transcriptional maturity early after acute ischemic cardiac injury

We subjected adult C57BL/6 mice to ischemic cardiac injury (Ubil et al., 2014) by permanent ligation of the left anterior descending coronary artery and observed acute and progressive loss of cardiac function (Fig S1A). Hearts were harvested at 3,7,14, 21 and 42 days after ischemic injury and the fibrotic scar tissue in the injured and region remote to the area of injury were dissected from the same heart for RNA-seq to quantify temporal changes in gene expression. Principal component analysis (PCA) showed samples from remote regions at all timepoints clustered together (Fig 1A). Principal component 1 (PC1) separated transcriptional signatures of injured and uninjured regions across all time points examined (Fig 1A) suggesting that gene expression differences continue to persist between the injured and uninjured regions. PC2 separated the samples of scar tissue in a temporal manner following injury (Fig 1A). In particular, significant differences were observed between scar tissue harvested at 3 and 7 days following injury as well as between that harvested at 7 days and subsequent time points. However, the transcriptional signatures of the injured region of the hearts at 14, 21 and 42 days after injury clustered together demonstrating that most transcriptional changes occur within 2 weeks of injury (Fig 1A). Analysis of differential expressed genes (DEG) demonstrated that the largest number of DEGs occurred between injured and uninjured samples at each analyzed timepoint (from 1210 to 1931) (Fig 1B, Table S1). Comparisons between time-points of injured regions detected 247 and 100 DEGs between day 3 and day 7, and day 7 and day 14 respectively. Almost no differences were detected between scar tissue harvested at later timepoints (Fig 1B). These data demonstrate that major transcriptional changes within scar tissue occur early after injury and further maturation of scar tissue beyond 2 weeks is not associated with significant transcriptional changes.

We hypothesized that genes that directly regulate scar size are upregulated early after ischemic cardiac injury. Collagens were one of the most differentially upregulated genes in the injured region early after injury. We examined expression pattern of genes encoding obligatory subunits of all types of collagen (Fig 1C). In addition to type I and III collagens, we observed genes encoding for various subunits of collagen V, VI, VIII, XI, XII, XIV, XV, XVI and XVIII to be significantly induced after heart injury (Fig 1C) with expression of most collagens increasing by 3 days, peaking at 7 days and declining by 42 days after injury (Fig 1C). Next, to confirm our findings, we performed qPCR for the principal genes encoding all mammalian collagens (Fig 1D, Fig S1B). *Col1a1* and *Col3a1* demonstrated the most robust gene expression changes after acute injury consistent with them being the principal cardiac collagens (Fig 1D). Collagen encoding genes that are known to be abundantly expressed in extra-cardiac tissues such as *Col2a1*, *Col7a1* and *Col9a2* demonstrated dynamic expression changes (Fig S1B), but absolute levels of expression was low (Fig S1C). Taken together, these data demonstrate that a diverse set of collagen genes including several that are minimally expressed in the uninjured heart are robustly induced early after acute ischemic cardiac injury.

Col5a1 expression overlaps *Col1a1* and *Col3a1* expression in the infarcted region with a single cardiac fibroblast expressing all three collagens

We next dissected the nascent scar tissue at 7 days following injury and first performed proteomic analysis of the collagens differentially expressed between the scar and uninjured tissue (Fig 2A). We confirmed increased levels of the fibrillar collagen peptide chains COL1A1, COL3A1 and COL5A1 and other collagen peptides (Fig 2A). *Col1a1* and *Col3a1* genes were the most abundantly expressed fibrillar collagen genes in scar tissue at 7 days following injury, (Fig 2B). Out of other fibrillar collagens (II, V, XI), *Col5a1* was the only one that was induced robustly early in scar tissue (Fig 2B).

We next examined the spatial expression of the fibrillar collagens Col I, III and V. The objective of this experiment was to determine whether the same cell expressed all the three fibrillar collagens (I,III,V) or whether the collagens were expressed by different cells in scar tissue. To prevent cross reactivity of antibodies to different collagens and to facilitate accurate fluorophore colocalization, we chose to perform RNA-fluorescence in situ hybridization (RNA-FISH) to determine the spatial expression of *Col5a1* versus *Col1a1* or *Col3a1* post injury. RNA-FISH demonstrated robust and overlapping expression of *Col5a1* with either *Col3a1* or *Col1a1* mRNA in the injured region of the heart (Fig 2C) and we observed the same cell to express both *Col5a1* and *Col3a1/Col1a1* (Fig 2D). To confirm these observations, we performed RNA-FISH in mice with genetically labeled cardiac fibroblasts. For this purpose, mice expressing fibroblast Cre drivers (Col1a2CreERT or TCF21MerCreMer) were crossed with the lineage reporter Rosa26tdTomato mice(Acharya et al., 2011; Pillai et al., 2017; Zheng et al., 2002) and tamoxifen administered to induce genetic labeling of cardiac fibroblasts (Pillai et al., 2017; Ubil et al., 2014). RNA-FISH on hearts harvested at 7 days post injury demonstrated tdTomato labeled cardiac fibroblasts to express Col5a1(Fig 2E). As cardiomyocytes are known to express collagens(Heras-Bautista et al., 2019), we performed immunostaining for cardiac troponin I, but did not observe cardiomyocytes to express *Col5a1* (Fig 2F). To provide corroborative evidence, we next

performed single cell RNA-seq of the non-myocyte cell fraction of the injured region of the heart at 7 days post injury and observed significant overlap between *Col5a1* expression and *Col3a1* and *Col1a1* expression (Fig 2G). Taken together these observations demonstrate that collagen I, III and V have overlapping expression in the area of injury and that a single cardiac fibroblast has the ability to produce both collagen V and collagen I/III.

Mice deficient in type V collagen exhibit a paradoxical increase in fibrosis and scar size after heart injury

Homozygous deletion of *Col5a1* gene results in absence of functional collagen V protein in tissues and causes early embryonic lethality (Wenstrup et al., 2004). Mice heterozygous for Col5a1 deficiency exhibit increased fibrosis in their valves and myocardium at birth suggestive of a role of Col V in regulating ECM output(Lincoln et al., 2006). To determine the functional role of collagen V in the injured heart, we first crossed the Col1a2CreERT mice with *Col5a1* floxed mice (Sun et al., 2011). We administered tamoxifen to progeny mice for 5 days prior to injury and continued for seven days post injury to maximize labeling and generate Col5a1CKO mice. Control animals included littermates that lacked the Cre transgene but had both *Col5a1* alleles floxed and were injected with tamoxifen in an identical manner. RNA-FISH on the Col5a1CKO hearts demonstrated 66.6±17.8% reduction of *Col5a1* expression (mean±S.D. *$p<0.05$) (Fig S2A,B). We observed significant depression of cardiac contractile performance (EF and FS) by 7 days in the Col5a1CKO group following ischemic injury, that persisted throughout the next 6 weeks (mean± S.D., *$p<0.05$,) (Fig 3A,B) and this was associated with a strong trend towards chamber dilatation ($p=0.06$ for LVID(d) at 6 weeks post MI) (Fig 3B). Histology demonstrated that the area of fibrotic scar tissue was significantly greater by 1.5 fold in the Col5a1CKO compared to wild type littermates (mean±S.D., *$p<0.05$) (Fig 3C,D). To further analyze the wound healing response in Col5a1CKO animals, we determined the fraction of animals which exhibited mild, moderate or severe fibrosis after ischemic injury. We defined mild, moderate and severe fibrosis as scar surface area less than 20%, between 20% and 40% and greater than 40% of the left ventricular surface area respectively measured at 6 weeks following injury and observed that greater than 58% of the Col5a1CKO animals had severe fibrosis compared to approximately 12% of animals in control littermates (Fig 3E). There were no significant differences in interstitial fibrosis of the uninjured myocardium in Col5a1CKO and control mice (Fig S2C). As scars mature, collagen fibrils undergo cross linking within scar tissue and become less soluble. We found that the amount of insoluble collagen (surrogate for cross linked collagen) was increased by 254±64% (mean± S.D.; *$p<0.05$) in the Col5a1CKO group at 6 weeks post injury (Fig 3F). Collagen V is thought to initiate organization of Collagen I and III fibrils in the extracellular matrix and is intercalated between the staggered arrangement of collagen I and collagen III fibrils maintaining organization of the ECM(Wenstrup et al., 2004). We performed toluidine blue staining and observed the typical wavy nature of collagen fibrils compactly arranged in parallel in the injured control animal hearts, but the hearts from the Col5a1CKO animals showed a loose arrangement of collagen fibers (Fig 3G). We performed transmission electron microscopy and instead of the smooth parallel arrangement of collagen fibrils in scars of control animals, we observed fibrillar disarray with fibrils running at orthogonal axes to each other in the Col5a1CKO scars (Fig 3H,I). Collagen fibril diameters were significantly greater (Fig 3J,K)

and a histogram of the numbers of collagen fibrils versus their diameter demonstrated a rightward shift of the curve in Col5a1CKO mice (Fig 3L). Finally, we performed electron tomography and observed shorter length, irregular fibrillar structure and breaks in collagen fibrils in the Col5a1CKO scar compared to wild type scar (Fig 3M,N). Taken together these observations demonstrate that deletion of type V collagen leads not only in increased scar size but also results in grossly abnormal scar architecture.

As increased scar size in the post infarcted heart is associated with adverse phenotypes such as hypertrophy of cardiomyocytes in the border zone(Frangogiannis, 2017, 2019), we harvested hearts at 6 weeks following injury and observed significantly greater heart weight/body weight ratios of Col5a1CKO hearts compared to control littermates (mean±S.D., *p<0.05) with no significant differences in body weight alone (Fig S2D,E). Immunostaining for cardiac troponin I confirmed robust hypertrophy of cardiomyocytes abutting the margins of the scar (borderzone) in Col5a1CKO animals (FigS2F,G).

Validation of phenotype of collagen V deficiency in the injured heart using an alternative Cre driver

To validate our observations noted with the Col1a2Cre driver, we generated another conditional knockout of the *Col5a1* gene using the Tcf21MerCreMer driver (Tcf21MCM), Tcf21 being a specific marker of cardiac fibroblasts in the adult heart (Acharya et al., 2011; Kanisicak et al., 2016). The Tcf21MCM mice were crossed with the Col5a1 floxed mice and tamoxifen administered 5 days prior to injury and for 7 days following injury to create Tcf21MCM:Col5a1CKO mice. Controls included littermate animals that had both *Col5a1* alleles floxed but lacked the Cre transgene and were injected with tamoxifen in an identical manner. At 7 days post injury, *Col5a1* expression in the injury region of Tcf21MCM:Col5a1CKO decreased by almost 60.1±10.1% (mean ± S.D., *p<0.05) (Fig S3A,B). Tcf21MCM:Col5a1CKO mice exhibited significant decline in cardiac contractile function by 7 days of injury that persisted for the next 6 weeks (Fig S3C,D) and this was also associated with a trend towards greater chamber size (LVID) (Fig S3D). We observed a significant 1.5 fold increase in scar size in Tcf21MCM:Col5a1CKO animals versus control littermates (mean±S.D, *p<0.05) (Fig S3E,F). The fraction of animals that exhibited severe fibrosis (>40% surface area) was 40% in the Tcf21MCM:Col5a1CKO animals compared to approximately 11% in the control littermates (Fig S3G). The Tcf21MCM:Col5a1CKO animals exhibited significantly greater heart weight/body weight ratios at 6 weeks after injury (no change in body weight) (Fig S3H,I) and histology confirmed significantly greater myocyte hypertrophy (mean±S.D., *p<0.05) (Fig S3J,K). To exclude a potential role of tamoxifen in contributing to post injury contractile dysfunction, tamoxifen was administered in an identical manner to TCF21MCM mice but without the Col5a1 floxed alleles. No differences in cardiac function were observed within 1 and 2 weeks of injury following tamoxifen administration (Fig S4A). Taken together, these observations using an independent Cre driver mirror provide compelling evidence that deletion of type V collagen leads to an exacerbated fibrotic repair response.

To complement these observations, we subjected the Col5a1 heterozygous KO mice ($Col5a1^{+/-}$)(Wenstrup et al., 2004) to ischemic cardiac injury. Compared to wild type

littermates, the heterozygote Col5a1KO exhibited a significant reduction in cardiac contractile function by 1 and 2 weeks of injury and exhibited greater degree of cardiac hypertrophy as assessed by heart weight/body weight ratios (Fig S4B–D). The data presented earlier shows that scars rapidly attain transcriptional maturity and cardiac function is significantly compromised within 7 days of injury in the Col5a1CKO mice. Considering these observations, we postulated that the effects of Col5a1 deficiency on cardiac function early after cardiac injury may be related to its role in mediating an acute fibrotic repair response. To investigate this, we deleted Col5a1 after the acute phase of injury by administering tamoxifen from post injury day 4 for 10 days. We observed that the TCF21MCM:Col5a1CKO animals (with deletion of Col5a1 after the acute injury response) did not exhibit a reduction in cardiac function at 2 weeks after injury (Fig S4E). These observations suggest that type V collagen affects post injury cardiac function by playing a critical role in the early fibrotic repair response.

Col5a1 is a critical determinant of post injury heart function vis-á-vis other ECM genes

A large number of collagens and other ECM proteins are upregulated in the region of scarring (in addition to collagen V) and an argument can be made of the functional importance of collagen V vis-a-vis other ECM proteins. We adopted a population genetics approach to determine the relative functional importance of Collagen V in driving post injury cardiac function vis-a-vis other extracellular matrix genes. The hybrid mouse diversity panel (HMDP) comprises approximately 100 diverse inbred and recombinant strains of mice and each strain can be subjected to an identical environmental perturbation to determine the genetic factors underlying responses(Ghazalpour et al., 2012; Lusis et al., 2016). The individual mouse strains in the HMDP were subjected to continuous isoproterenol infusion for 3 weeks that induces a chronic form of cardiac injury characterized by cardiomyocyte hypertrophy and interstitial fibrosis (Wang et al., 2016). Key traits of cardiac function such as cardiac contractility, chamber size and fibrosis were followed over 3 weeks. Gene expression changes in the heart following isoproterenol infusion were determined in each strain and these were statistically integrated with clinical traits to identify key loci or genes involved (Fig 4A). (Rau et al., 2017; Rau et al., 2014). We first analyzed a set of extracellular matrix genes including collagens (Extracellular Matrix - GO:0031012 or Collagen Network - GO:0098645) that are abundantly expressed in the heart (Fig S4F) for correlations with clinical traits mentioned above (Fig 4B). *Col5a1* expression significantly correlated with cardiac traits of chamber size (LVID systole/diastole), cardiac hypertrophy (LV mass) and systolic and diastolic function (EF and E/A ratios) (Fig 4C–G). We also observed genetic variation in the average expression of Col5a1 across the strains in the HMDP (Fig S4G). We next analyzed the strength of association between *Col5a1* gene expression and the above mentioned set of extracellular matrix genes after isoproterenol. While several significant relationships were observed between *Col5a1* and ECM genes, there did not appear to be consistent patterns of overall positive or negative concordance (Fig 4H, Table S2). Given that (i) ECM genes strongly correlate with clinical traits and (ii) *Col5a1* gene expression strongly correlates with a subset of ECM genes, we performed conditional analyses to evaluate the functional importance of *Col5a1* in mediating ECM:trait correlations. If *Col5a1* significantly contributed to the strength of correlation between ECM genes and traits, then adjustment for *Col5a1* expression should reduce the overall

significance of correlations (Fig 4I). Conditioning on *Col5a1* expression led to a significant reduction in the overall strength of the association between rest of ECM genes and cardiac traits of chamber size, LV mass and EF while measures of diastolic compliance (E/A ratio) were not affected following *Col5a1* adjustment (Fig 4J). To test whether the correlation was specifically dependent on *Col5a1,* we conditioned on each of the other ECM genes and then assessed the change in significance of the correlations. As can be seen In Fig 4K–N, that while conditioning on several genes reduced the strength of the correlations, *Col5a1* showed the highest changes in significance following adjustment for LVID (systole), LVID (diastole) and ejection fraction. Only for cardiac mass, was *Col5a1* in ranked second after *Col1a1* (Fig 4M). Using alternative cardiac injury models and complementary genetics approaches, these data support our principal observations of the physiological importance of collagen V in regulating heart repair.

Collagen V deficiency increases myofibroblast formation and expression of extracellular matrix genes in scar tissue

We next investigated mechanisms by which *Col5a1* deficiency leads to increase in scar size and examined whether the deficiency of *Col5a1* altered cell populations in the scar or affected their transcriptional signatures. As maximal changes in transcriptional signatures of scars occur within the first few days after cardiac injury (Fig 1A), we harvested injured and uninjured regions of hearts, isolated non-myocyte cells and subjected the cells to single cell RNA-seq using the 10X genomics platform. A tSNE (t-distributed stochastic neighbor embedding) plot demonstrated the major cell populations in the injured region at 7 days (Fig 5A, Fig S5A). We next determined the fraction of cells contributing to each cluster in the Col5a1CKO and wild type controls (Fig 5B) and observed a comparable distribution of cells across fibroblast, endothelial, smooth muscle and other cell populations with a slightly higher number of macrophages (Fig 5B, Fig S5B). As *Col5a1* was deleted principally in cardiac fibroblasts, we focused on DEGs in the cardiac fibroblast cell cluster and first confirmed decreased expression of *Col5a1* in fibroblasts from Col5a1CKO mice (Fig 5C). We observed that fibroblasts from Col5a1CKO hearts exhibited significantly greater expression of *Acta 2* (αsmooth muscle actin or αSMA) (Fig 5D), a gene that is not expressed by cardiac fibroblasts in the uninjured heart but is a marker of myofibroblasts, a population of activated fibroblasts expressing smooth muscle contractile proteins(Frangogiannis, 2019). Myofibroblasts exhibit a synthetic and contractile phenotype and are thought to be the principal cells that secrete ECM proteins to form scar tissue (van den Borne et al., 2010). Other smooth muscle specific contractile proteins (*Cnn2* (calponin), *Actn1* (Actinin 1), markers of smooth muscle differentiation SM22α (*Tagln*), proteins regulating smooth muscle contraction such as regulatory myosins (*Myl 6*, *Myl9*) or calcium handling during smooth muscle contraction (*S100a4,s100a6*) were also significantly upregulated in fibroblasts of Col5a1CKO animals suggestive of broad cytoskeletal organization and activation of fibroblasts (Fig 5E, Fig S5C). Lysyl oxidase (*Lox*), that mediates cross linking of collagen was also upregulated (Fig S5C) consistent with increased amounts of insoluble collagen in scar tissue of Col5a1CKO hearts. We next examined the subsets of fibroblasts residing within the fibroblast cluster (Fig 5F) and observed that *αSMA* was abundantly expressed in Cluster0 identifying that cluster as a population enriched in myofibroblasts (Fig 5G,H). We observed that the number of myofibroblasts (defined as

fibroblasts expressing *αSMA*) (Cluster 0) was significantly increased by 33% in the Col5a1CKO animals (Fig 5I). To confirm these findings, we performed double immunofluorescence staining for αSMA and vimentin (fibroblast marker) on hearts of Col5a1CKO mice and observed that the number of myofibroblasts (defined as the fraction of αSMA+vimentin+/total number of vimentin+ cells) was 2-2.5 fold greater in the scar tissue of Col5a1CKO mice (Fig 5J,K) or that of Tcf21MCM:Col5a1CKO mice (Fig 5L,M) (mean ±S.D.,*p<0.05). Analysis of differentially expressed ECM genes demonstrated a large number of ECM genes to be significantly upregulated in Col5a1CKO fibroblasts including several collagens (*Col8a1*, *Col11a1*), fibronectin, osteopontin and *fibrillin* (Fig 5N). Our data suggests that increased numbers of myofibroblasts along with increased expression of myofibroblast markers and other ECM genes in cardiac scar tissue of Col5a1CKO animals contribute to the increase in scar size. We next determined whether increased myofibroblast numbers in Col5a1CKO scar tissue were secondary to increased proliferation. We examined the expression of cell cycle genes that regulate S/G1 as well as G2/M transitions of the cell cycle in Cluster 0 (myofibroblast population) (Fig S6A,B) but the average expression of such genes did not show any difference between the myofibroblasts of control and Col5a1CKO animals (Fig S6C). We performed immunostaining for a marker of proliferation (Ki67), but also did not observe any significant differences between the fraction of fibroblasts expressing Ki67 (Fig S6D). Collectively, these observations suggest that increased myofibroblast differentiation/formation rather than myofibroblast proliferation likely underlies the increased myofibroblast numbers observed in Col5a1CKO scar tissue compared to that of control littermates.

Collagen V deficiency alters mechanical properties of fibroblasts and matrix in scar tissue.

We next explored the molecular underpinnings of increased myofibroblast differentiation and hypothesized that altered mechanical properties of the matrix could be driving feedback cues to drive myofibroblast differentiation. We first performed atomic force microscopy (AFM) to determine the stiffness of mid ventricular scar tissue scar tissue 7 days post injury and observed that the Young's modulus was significantly decreased by 15% in the Col5a1CKO animals (Fig 6A–D) and a less stiff scar is more prone to expansion by hemodynamic forces. Scar contraction is another major determinant of scar size. During wound healing, contractile forces generated by cardiac fibroblasts shrink the size of the scar but if the surrounding matrix is less stiff, this would decrease the forces transduced through scar tissue. We explored this hypothesis by examining force contraction relationships of mutant and control fibroblasts isolated from scar tissue at 7 days following injury. We fabricated a device with polydimethyl siloxane (PDMS) posts, isolated cardiac fibroblasts from infarcted hearts, incorporated the fibroblasts into a collagen hydrogel to form tissue scaffolds and subsequently suspended the fibroblast-embedded hydrogel between two PDMS posts (Fig 6E). We observed a significantly lower displacement of the PDMS posts with the Col5a1CKO fibroblasts, that reflects decreased contractile ability of Col5a1CKO fibroblasts (approximately 34% reduction, *p<0.05) (Fig 6F–H). Next, we isolated cardiac fibroblasts from Col5a1 floxed mice and infected the cardiac fibroblasts in-vitro with a lenti-virus encoding Cre recombinase gene or GFP as control (Fig 6I). To minimize artifacts from repeated passaging, we immortalized the isolated Col5a1fl/fl cardiac fibroblasts by infecting them with a lentivirus encoding the SV40 large T cell antigen, prior to infecting the cells

with Cre recombinase or control GFP virus(Mali et al., 2008; Welm et al., 2008). Cells infected by Cre recombinase lentivirus(Truitt et al., 2016) were identified by co-expression of GFP fluorescence and sorted by flow cytometry and we found approximately 60±20% decrease in *Col5a1* expression (mean±S.D. *p<0.05). Successfully transduced cells were then incorporated into collagen hydrogels and suspended between PDMS posts in a similar manner. We observed a significant reduction in pillar displacement and hydrogel contraction suggestive that the deficiency of ColV is sufficient to affect fibroblast contractile forces (Fig 6J,K). Taken together these experiments show that ColV depletion leads to decreased scar stiffness and attenuated tissue scaffold contraction by fibroblasts, which could both contribute to increased scar size.

To assay the mechanical properties of fibroblasts, we subjected the Col5a1floxed cardiac fibroblasts (following lenti Cre infection) to a cell deformability assay. In this assay, cell deformability is determined by parallel microfiltration (PMF), where the ability of cells to filter through a porous membrane over the timescale of seconds in response to an applied pressure is determined (Kim et al., 2016; Kim et al., 2019; Qi et al., 2015). More deformable cells will filter more quickly through the pores resulting in a lower volume of cell suspension retained in the top well (Fig 6L). We observed that Col5a1CKO fibroblasts are significantly less deformable (Fig 6M) while there were no significant differences in cell size or viability between lenti Cre or lenti GFP cardiac fibroblasts (Fig S7A,B). To further investigate the altered physical properties of Col5a1CKO fibroblasts, we performed quantitative phase microscopy (QPM) to measure the rate at which biomass redistributes within individual cells (decorrelation rate). We observed that the decorrelation rate was faster (approximately two fold higher) in Col5a1CKO fibroblasts versus control-GFP virus infected fibroblasts (mean±S.D. *p<0.05,) (FigS7C–E), further substantiating the altered physical properties of Col5a1CKO fibroblasts.

We next examined whether stiffer cardiac fibroblasts affect cardiomyocyte contractile forces thereby reducing cardiac function. We co-cultured neonatal rodent ventricular cardiomyocytes (NRVM) with Col5a1 deficient or control cardiac fibroblasts generated *in vitro*. We performed traction force microscopy to determine myocyte contractile forces generated in the presence of control of Col5a1CKO cardiac fibroblasts. A co-culture of cardiomyocytes and control or Col5a1CKO cardiac fibroblasts was seeded onto a Matrigel surface on a PDMS scaffold containing gold labeled nano-particles (Fig 6N). As the myocytes contract, the movement or displacement of the gold particles are captured and then machine learning approaches utilized to calculate contractile forces (Fig 6O). Using this approach, we observed that the stress generated by myocytes in the presence of Col5a1CKO fibroblasts is significantly decreased (Fig 6P) (mean±S.D. *p<0.05). These observations are consistent with our in-vivo findings of decreased cardiac contractile forces in Col5a1CKO hearts following ischemic cardiac injury.

Collagen V deficiency induces myofibroblast formation via altered integrin expression on cardiac fibroblasts

Given the abnormal biomechanical properties of the scar, we hypothesized that altered mechanical cues were driving a myofibroblast gene expression program and increasing

myofibroblast formation. First, we determined whether the deficiency of Col5a1 in cardiac fibroblasts was sufficient to induce myofibroblast differentiation and expression of ECM genes. To address this question, we again generated Col5a1 deficient cardiac fibroblasts by lentiviral Cre transduction and observed significant upregulation of canonical myofibroblast and ECM genes such as *aSMA, periostin, Col3a1, Myh11* etc (Fig 7A). These observations demonstrate that the loss of *Col5a1* is sufficient to induce activation of a myofibroblast gene expression program. Integrins are mechanosensitive receptors on the cell surface and alterations in mechanical properties of the extracellular environment can lead to rapid changes in integrin profile. Moreover, integrins are known to regulate key cellular events such as cell survival, proliferation and differentiation(Hynes, 2002; Katsumi et al., 2004). We hypothesized that augmentation of a myofibroblast gene expression program in Col5a1CKO fibroblasts could be secondary to altered integrin expression on the *Col5a1CKO* fibroblasts. We performed flow cytometry on *Col5a1* deficient cardiac fibroblasts and observed that a significant greater fraction of *Col5a1* deficient cardiac fibroblasts expressed the integrins αvβ3 and αvβ5 (Fig 7B,C). In contrast, β1, β2, α5 and αv integrins did not show any changes in expression (Fig S7F–I). These integrins were chosen as they have shown to affect smooth muscle and fibroblast function(Deb et al., 2004; Ieda et al., 2009; Liu et al., 2010), and in particular for αvβ3/αvβ5, there is evidence that these integrins promote myofibroblast differentiation by modulating latent TGFβ signaling(Asano et al., 2005; Lygoe et al., 2004; Sarrazy et al., 2014).

Immunostaining demonstrated robust expression of αvβ3 and αvβ5 integrins in cardiac fibroblasts of Col5a1CKO scar tissue compared to that of control littermates (Fig 7D,E). Myocardium remote to the area of injury did not show any expression of αvβ3 and αvβ5 integrins (Fig S8A). Given the upregulation of αvβ3 and αvβ5 integrins in Col5a1CKO cardiac fibroblasts, we next determined whether there was a causal relationship between these differentially expressed integrins and myofibroblast differentiation. To address this question, we adopted a pharmacologic loss of function approach by using the drug cilengitide, a specific inhibitor of αvβ3 and αvβ5 integrins. Cilengitide is a cyclic Arg-Gly-Asp peptide that has been used in human clinical trials of various malignancies such as gliomas, and is a specific inhibitor of the αvβ3 and αvβ5 integrins(Belvisi et al., 2005; Dechantsreiter et al., 1999; Scaringi et al., 2012). We infected the Col5a1 floxed cardiac fibroblasts with a lentiviral Cre or control GFP and added cilengitide to cardiac fibroblasts at the same time. After 7 days, expression of myofibroblast markers was significantly increased in the Col5a1CKO fibroblasts but the addition of cilengitide significantly reduced expression of myofibroblast markers (Fig 7F).

Considering these observations, we investigated the effects of injecting cilengitide *in vivo* to Col5a1CKO animals to determine effects on post injury scar size and cardiac function. We subjected Col5a1CKO to ischemic cardiac injury and injected cilengitide or vehicle at 20mg/kg daily (Bagnato et al., 2018) for 14 days starting from the day of injury (Fig 7G). We observed that the Col5a1CKO animals injected with vehicle exhibited a significant decline in post injury cardiac function, but the Col5a1CKO animals treated with cilengitide had a complete rescue of function and the post injury heart function was not significantly different from the control littermates (Cre(-)Col5a1$^{fl/fl}$) (Fig 7H,I) In contrast, cilengitide infusion did not affect post injury cardiac function of control (Cre(-)Col5a1$^{fl/fl}$) littermate

animals (Fig 7H). Histology demonstrated significant reduction in scar size in Col5a1CKO animals injected with cilengitide compared to vehicle injected Col5a1CKO animals (Fig 7J,K). To demonstrate that the benefits of cilengitide on post injury cardiac function of Col5a1CKO animals was secondary to its effect on the infarcted region, we performed myocardial strain imaging. Longitudinal strain generated by different segments of myocardial walls is a surrogate for contractile forces generated. With myocardial infarction the basal segment of the myocardium close to the suture line was relatively unaffected compared to the anterior apical wall (Fig S8B,C). Following cilengitide administration, the functional improvement was restricted to the apical segment and not the basal segment demonstrating that the beneficial effects of cilengitide were not secondary to augmentation of contractile forces of the non-injured myocardium (Fig S8D). Cilengitide did not affect the scar size of control animals [Cre(-)Col5a1$^{fl/fl}$] following injury (Fig 7J,K). The Col5a1CKO animals injected with cilengitide had a much lower fraction of animals exhibiting severe fibrosis (Fig 7L). We next examined the numbers of myofibroblasts in the scars of Col5a1CKO animals and observed that the number of myofibroblasts was significantly reduced in the cilengitide group (Fig 7M). We subsequently determined whether cilengitide reversed increased expression of ECM genes in cardiac fibroblasts of Col5a1CKO animals. We examined the set of ECM genes that were upregulated in cardiac fibroblasts in Col5a1CKO hearts at 7days following injury. Single cell RNA-seq of fibroblasts isolated from Col5a1CKO hearts following 7 days of cilengitide therapy demonstrated reversion of expression of these genes and average expression of this module of genes was significantly lower in cardiac fibroblasts following cilengitide treatment (p=9.3e-7; Fig 7N,O). The degree of myocyte hypertrophy was also substantially reduced in the cilengitide injected Col5a1CKO animals (Fig S8E,F). Taken together these experiments demonstrate that the differential expression of αvβ3 and αvβ5 integrins in cardiac fibroblasts of Col5a1CKO animals drives myofibroblast differentiation and pharmacologic inhibition of such integrins is sufficient to rescue the phenotype.

Discussion

Our data can be used to construct a collagen V dependent model of cardiac wound healing where collagen V regulates wound healing at least in part by modulating the mechanical properties of the scar. In the absence of collagen V, the scar is less stiff and less stiff scars are prone to sudden scar expansion (Rog-Zielinska et al., 2016). In addition, the reduced scar stiffness drives integrin mediated mechanical feedback cues that promote myofibroblast differentiation, further ECM production and scar size. The feedback response is critical to the phenotype as modulation of specific integrin signaling reverses increased ECM gene expression and rescues the phenotype.

Our findings could also have implications for Ehlers Danlos syndrome (EDS), a heterogeneous group of connective tissue disorders characterized by abnormalities in skin extensibility, joint hypermobility and tissue fragility(Ghali et al., 2019). Individuals with classical EDS (cEDS) most commonly have mutations in genes encoding for type V collagen (*Col5a1*,*Col5a2*) (Wenstrup et al., 2000). Although there is scant clinical data on the prognosis of MI and heart scarring in these patients (owing to the relatively rare nature of the disease), patients with cEDS have abnormal mechanical properties of the ECM and

exhibit dysregulated wound healing with increased scar size. Moreover, fibroblasts isolated from skin of patients with cEDS demonstrate increased expression of αvβ3 integrins (Zoppi et al., 2018) that is thought to reflect a response to abnormal ECM and raise the possibility that inhibitors of specific integrins such as cilengitide may have a role in mitigating dysregulated wound healing in cEDS.

In summary, we demonstrate that a feedback mechanism between the mechanical properties of scar tissue and cardiac fibroblasts are pivotal to the regulation of scar size. Teleologically, such a feedback loop provides an efficient way to integrate the output of ECM and strength of scars. Our observations illustrate a model of wound healing, where the structural constituents of scar tissue function to limit the size of scar itself.

STAR Methods

Resource Availability

Lead Contact—Further information and requests for resources and reagents should be directed to and will be fulfilled by the Lead Contact, Arjun Deb (adeb@mednet.ucla.edu)

Materials Availability—This study did not generate new reagents.

Data and Code Availability—The accession number for the bulk RNA sequencing and single-cell RNA sequencing in this paper are available in NCBI GEO dataset. Myocardial infarction bulk RNAseq data: GSE151834, Myocardial infarction sc RNAseq data: GSE152122, Myocardial infarction sc RNAseq data from Col5a1CKO/Control mouse: GSE151695, Myocardial infarction sc RNAseq data from Col5a1CKO mouse treated with cilengitide or vehicle: GSE151695.

Figures for STAR Methods are available in Mendeley data (DOI: 10.17632/z3vsb9yvks.2)

Experimental Model and Subject Details

Animal care and use—All animal studies were approved by the Animal Research Committee, University of California, Los Angeles. All animals were maintained at the UCLA vivarium according to the policies instituted by the American Association for Accreditation of Laboratory Animal Care. Sample size was estimated based on published literatures on murine myocardial infarction models(Hinkel et al., 2015; Ren et al., 2005). Male and female animals aged between 10 and 14 weeks were used in the study. All animals belonged to the C57Bl/6 strain, were healthy, immune-free, and drug or test naïve and were not involved in other experimental procedures. Littermates were used as controls for all experiments.

Generation of animals with genetically labeled cardiac fibroblasts and fibroblast specific deletion of Col5a1.—Col1a2CreERT (B6 background) and TCF21MerCreMer (B6 background) animals were crossed with the lineage reporter Rosa26tdtomato (B6 background) animals to generate progeny animals as described(Pillai et al., 2017). Tamoxifen was administered for 10 days prior to ischemic cardiac injury followed by RNA-FISH to determine whether genetically labeled fibroblasts co-expressed the RNA

signal. For generation of Col5a1CKO mice, Col1a2CreERT or TCF21MerCreMer mice were crossed with the Col5a1 floxed (B6 background) mice (Sun et al., 2011) and progeny mice were administered tamoxifen (1 mg IP daily) for 5 days prior to ischemic injury and continued for 7 days following injury. For the experiment on TCF21MerCreMer mice to demonstrate an effect of Cre recombinase on heart function and fibrosis, these mice were administered tamoxifen for 5 days prior to ischemic injury and continued for 7 days following injury as as for generating Col5a1CKO mice. For experiments related to administration of tamoxifen after acute injury, TCF21MerCreMer mice crossed with the Col5a1 floxed mice were administered tamoxifen from 4 days to 14 days post injury. Col5a1(+/−) heterozygous KO (B6 background) mice (Lincoln et al., 2006) were used for experiments to confirm Col5a1CKO post infarction phenotype.

Murine models of acute ischemic cardiac injury—All animal studies were approved by the Animal Research Committee, University of California, Los Angeles. Myocardial infarction was performed by ligating the left anterior descending (LAD) coronary artery following open thoracotomy as described(Pillai et al., 2017; Ubil et al., 2014). Briefly, Mice were anesthetized with ketamine (80 mg/kg)/xylazine (20 mg/kg) by intraperitoneal injection. Respiration was provided by mechanical ventilation with 95% O2 (tidal volume 0.5 ml, 130 breaths/min). The LAD coronary artery was ligated intramurally 2mm from its origin with a 9-0 proline suture.

For experiments related to use of cilengitide, 20mg/kg of Cilengitide diluted in PBS was administered by intraperitoneal injection every day until harvest and PBS was used as vehicle as a control.

Echocardiogram—Animals was assessed at pretreatment baseline and at the time point of 3 day, 1 week, 2 weeks, 3 weeks, 4 weeks, and 6 weeks post-Myocardial infarction. Animals were continuously anesthetized with 1.5% isoflurane and 95% O2. Vevo2100 imaging system and a 30-mHz scan head (Toronto, Canada) were used to acquire short/long axis B-mode and M-mode images. Long axis B-mode view was used for analyzing peak longitudinal strain rate. All measurements and calculations were conducted using Vevo2100 software.

Method Details

Antibodies and probes—The following primary antibodies, reagents, or probes were used for immunostaining: rabbit anti-Vimentin (1:100, Abcam, ab45939); mouse anti-smooth muscle actin (1:100, Dako, M0851); anti-cardiac Troponin I (1:100, Abcam, ab47003); mouse anti-integrin αVβ3 (1:50, Abcam, ab7166); mouse integrin αVβ5 (1:20, R&D, MAB2528); Alexa Fluor 594 conjugated WGA (5μg/ml, Invitrogen, W11262). For dual RNA-FISH/immunostaining: rabbit anti-RFP (1:50, Rockland, 600-401-379). For flowcytometry: rabbit anti-integrin αVβ3(CD51/CD61) (1:100, ThermoFisher, MA5-32195); rabbit anti-integrin αVβ5 (1:30, Bioss, bs-1356R); PE-conjugated rat anti-integrin αV (1:20, Invitrogen, 12-0512-82); PE-conjugated rat anti-integrin β1 (1:20, Invitrogen, 12-0181-82); PE-conjugated american hamster anti-integrin β2 (1:20, Invitrogen, 12-0291-82); PE-conjugated rat anti-integrin α5 (1:100, BioLegend, 103805); PE-

conjugated rat IgG isotype control (same dilution for target antibody, BioLegend, 400508). For RNA-FISH: mouse Col1a1-C1 probe (1:50, ACD, 319371); mouse Col3a1-C2 probe (1:50, ACD, 455771-C2); mouse Col5a1-C3 probe (1:50, ACD, 521291-C3).

Bulk RNA-seq, single-cell RNA-seq and qPCR—For bulk RNA-seq, the injured and uninjured regions of the heart were harvested at different time points following injury, total RNA extracted using RNeasy Mini kit (Qiagen) and used to generate RNA-Seq libraries followed by sequencing using Illumina 4000 platform (single-end, 65bp). Reads were aligned to the mouse reference genome (mm10) using STAR aligner (Dobin et al., 2013), and used to quantify normalized expression values (RPKM) for annotated genes (Ensembl v.86). RPKM values were used for principal component analysis (PCA) and gene expression visualizations. Differential expression analysis was performed using edgeR quasi-likelihood pipeline(Robinson et al., 2010). Differential expressed genes (DEGs) were identified at FDR 1% and minimum fold-change value of 4.

For sc- RNA-seq, 1wk post MI hearts were harvested and digested by liberase as described later. After digestion, cells were incubated with 10μM Calcein AM (Abcam, ab141420) and flow sorted to identify live cells followed by library preparation. Library was generated by Chromium™ Single Cell 3' Library Construction (10x Genomics) and sequenced by Illumina NextSeq 500 Sequencing System. After sequencing, fastq files were generated using Cellranger mkfastq (version 3.0.2). The raw reads were mapped to human reference genome (refdata-cellranger-mm10-3.0.0) using cellranger count. Digital expression matrix was extracted from the filtered_feature_bc_matrix folder outputted by the cell ranger count pipeline. Multiple samples were aggregated by cellranger aggr. To identify different cell types and find signature genes for each cell type, the R package Seurat (version 3.0.2) was used to analyze the digital expression matrix. Cells with less than 500 unique molecular identifiers (UMIs) or less than 100 genes, or greater than 50% mitochondrial expression were removed, resulting in a final dataset of 17,826 cells and 21,447 genes for further analysis. The Seurat function NormalizeData was used to normalize the raw counts. Variable genes were identified using the FindVariableFeatures function. The ScaleData function was used to scale and center expression values in the dataset, the number of unique molecular identifiers (UMI) was regressed against each gene. Principal component analysis (PCA), t-distributed stochastic neighbor embedding (tSNE), and uniform manifold approximation and projection (UMAP) were used to reduce the dimensions of the data, and the first 2 dimensions were used in the plots. The FindClusters function was sued cluster the cells.

Marker genes were found using the FindAllMarkers function for each cluster. Cell types were annotated based on the marker genes and their match to canonical markers. For qPCR, For RNA-seq, the injured and uninjured regions of the heart were harvested at different time points following injury, RNA extracted using RNeasy Mini kit (Qiagen). cDNAs were generated using iScript cDNA Synthesis Kit (BioRad) and qPCR performed.

Col5a1 correlation with extracellular matrix pathway accounts for clinical trait association in the HMDP—The data used for analysis, including left ventricle expression arrays and clinical traits can be found using the GEO accession: GSE48760 and within the following studies [5, 6]. Midweight bicorrelation coefficients and corresponding

p-values were generated from HMDP data using the R package WGGNA. To calculate adjusted regressions using the same approaches and compare directly, residuals from each ECM gene correlated with Col5a1 were extracted from the regression using the base lm() function in R. These residuals were then integrated with original expression values and correlated against indicated traits also using WGCNA to enable direct comparisons. For purposes of comparisons, we also adopted a similar approach by collapsing all ECM genes into eigengenes using WGCNA and correlated with either traits or traits adjusted for Col5a1 expression. Distributions of p-values resulting from these analyses were compared using a students t-test (two-way). Plots for visualization were made sing either ggplot2 or pheatmap packages in R.

Proteomic analysis of scar tissue—Injured and uninjured regions of the mouse heart at Day 7 following injury were dissected and homogenized in lysis buffer (200 uL, 12 mM sodium lauroyl sarcosine, 0.5% sodium deoxycholate, 50 mM triethylammonium bicarbonate (TEAB)), Sigma Protease Inhibitor Cocktail (0.89 mg/mL final concentration)), then subjected to bath sonication (10 min, Bioruptor Pico, Diagenode Inc. (Denville, NJ)) and heated (95 °C, 5 min). An aliquot of the resulting solution (9 uL) was taken for measurement of total protein concentration (bicinchoninic acid assay; Micro BCA Protein Assay Kit, Thermo Fisher Scientific, Waltham, MA, using BSA as a standard). The remaining samples were diluted to 0.5 mg protein/mL with lysis buffer, and an aliquot of each (100 uL) was treated with tris(2-carboxyethyl) phosphine (10 uL, 55 mM in 50 mM TEAB, 30 min, 37 °C) followed by treatment with chloroacetamide (10 uL, 120 mM in 50 mM TEAB, 30 min, 25 °C in the dark). They were then diluted 5-fold with aqueous 50 mM TEAB, and incubated overnight with Sequencing Grade Modified Trypsin (1 ug in 10 uL of 50 mM TEAB; Promega, Madison, WI) following which an equal volume of ethyl acetate/trifluoroacetic acid (TFA, 100/1, v/v) was added. After vigorous mixing (5 min) and centrifugation (13,000 x g, 5 min), the supernatants were discarded and the lower phases were dried in a centrifugal vacuum concentrator. The samples were then desalted using a modified version of Rappsilber's protocol (Rappsilber et al., 2007) in which the dried samples were reconstituted in acetonitrile/water/TFA (solvent A, 100 uL, 2/98/0.1, v/v/v) and then loaded onto a small portion of a C18-silica disk (3M, Maplewood, MN) placed in a 200 uL pipette tip. Prior to sample loading the C18 disk was prepared by sequential treatment with methanol (20 uL), acetonitrile/water/TFA (solvent B, 20 uL, 80/20/0.1, v/v/v) and finally with solvent A (20 uL). After loading the sample, the disc was washed with solvent A (20 uL, eluent discarded) and eluted with solvent B (40 uL). The collected eluent was dried in a centrifugal vacuum concentrator. The samples were then chemically modified using a TMT10plex Isobaric Label Reagent Set (Thermo Fisher Scientific) as per the manufacturer's protocol. The TMT-labeled peptides were dried and reconstituted in solvent A (50 uL), and an aliquot (2 uL) was taken for measurement of total peptide concentration (Pierce Quantitative Colorimetric Peptide, Thermo Fisher Scientific). The samples were then pooled according to protein content (10 ug of peptide from each sample; 100 ug total), and desalted using the modified Rappsilber's protocol described above. The dried multiplexed pooled sample was reconstituted in water/acetonitrile with 10mM ammonium bicarbonate (solvent C, 5uL, 98/2, v/v, pH10) prior to fractionation (2.7 uL injection) via high pH reversed-phase chromatography using a 1260 Infinity LC System (Agilent Technologies,

Santa Clara, CA) and a ZORBAX 300 Extend-C18 column (Agilent Technologies, 0.3 × 150 mm, 3.5 μm) equilibrated in solvent C and eluted (6 uL/min) with an increasing concentration of solvent D (acetonitrile/water with 10mM ammonium bicarbonate, 80/20, v/v, pH10: min/% D; 0/0, 5/14, 65/60, 75/0, 95/0). The fractions were eluted into a 96-well plate with 20 uL of 5% formic acid (FA) in each well over the course of 68 minutes. The 96 fractions were then condensed into 12 fractions prior to another desalting again using the modified Rappsilber's protocol described above. The eluants were then dried and reconstituted in water/acetonitrile/FA (solvent E, 10 uL, 98/2/0.1, v/v/v), and aliquots (5 uL) were injected onto a reverse phase nanobore HPLC column (AcuTech Scientific, C18, 1.8um particle size, 360 um x 20 cm, 150 um ID), equilibrated in solvent E and eluted (500 nL/min) with an increasing concentration of solvent F (acetonitrile/water/FA, 98/2/0.1, v/v/v: min/% F; 0/0, 5/3, 18/7, 74/12, 144/24, 153/27, 162/40, 164/80, 174/80, 176/0, 180/0) using an Eksigent NanoLC-2D system (Sciex (Framingham, MA)). The effluent from the column was directed to a nanospray ionization source connected to a hybrid quadrupole-Orbitrap mass spectrometer (Q Exactive Plus, Thermo Fisher Scientific) acquiring mass spectra in a data-dependent mode alternating between a full scan (*m/z* 350-1700, automated gain control (AGC) target 3 x 10^6, 50 ms maximum injection time, FWHM resolution 70,000 at m/z 200) and up to 10 MS/MS scans (quadrupole isolation of charge states ≥ 2, isolation width 1.2 Th) with previously optimized fragmentation conditions (normalized collision energy of 32, dynamic exclusion of 30 s, AGC target 1 x 10^5, 100 ms maximum injection time, FWHM resolution 35,000 at *m/z* 200). The raw data was analyzed in Proteome Discoverer 2.2, which provided measurements of relative abundance of the identified peptides.

Histological studies—Hearts were harvested under anesthesia and perfused with PBS followed by fixation in 4%formaldehyde in PBS at 4°C for 24 h, and subsequently subjected to dehydration in sucrose solution. Then the hearts were embedded in Tissue-Tek O.C.T compound (SAKURA, Finetek, USA) and sectioned with 10αm-thickness.

For immunostaining, tissue sections were incubated with pre-chilled acetone at −20°C for 10 min, blocked in 10% species-specific normal serum in 1% BSA/PBS for 1 h, and primary antibodies diluted in 1% BSA/PBS at 4°C overnight. Secondary antibodies were diluted in PBS and incubated with the sections for 1 h. Samples were counterstained with DAPI (1μg/mL, Invitrogen, D3571) and mounted with SlowFade Gold Antifade reagent (Invitrogen, S36936). Images were taken using Nikon Eclipse Ti2 confocal microscopy (Nikon,USA) and analyzed in NIS Element AR software (Nikon). For detection of αsmooth muscle actin, integrin αVβ3, and αVβ5, M.O.M immunodetection kit (Vector) was used. Breifly, tissue sections were incubated with pre-chilled acetone at −20°C for 10 min, incubated with Avidin/Biotin blocking buffer (Vector) for 15 min, M.O.M blocking buffer for 1 h, and primary antibodies diluted in M.O.M diluent at 4°C overnight. Biotinylated 2nd antibody against mouse (Vector) was diluted in M.O.M diluent (1:250) and incubated with the sections for 10 min. Samples were incubated with diluted fluorescien avidin DCS (1:60) for 5 min. Samples were counterstained with DAPI (1μg/mL, Invitrogen, D3571) and mounted with SlowFade Gold Antifade reagent (Invitrogen, S36936).

For Masson Trichrome staining, sections were stained using Masson Trichrome Stain kit (Thermo Scientific, 87019). Images were taken in heart sections from apex, mid-ventricle,

and close to suture and fibrotic area analyzed from apex to mid-ventricle. Scar tissue area was calculated as the fraction of left ventricular surface area occupied by the scar tissue. Severity of fibrosis was classified as sample showed >40% fibrotic area as “severe”, 20-40% as “moderate”, or <20% as “mild” for 6wks post MI hearts and >50% fibrotic area as “severe”, 30-50% as “moderate”, or <30% as “mild” for 2wks post MI hearts.

RNA-Fluorescence in situ hybridization.—RNA-FISH was performed using RNAscope Multiplex Fluorescent reagent kit v2 (ACD Inc, USA) as per manufacturer instructions. Tissue sections were incubated with hydrogen peroxide for 15 minutes followed by incubation with RNAscope Target Retrieval Reagent at 99°C for 5 minutes. Then the section was incubated with Protease III reagent at 40°C for 30 minutes in HybEZ II oven (ACDInc). After pre-treatment steps, RNAscope probes were hybridized at 40°C for 2 h, AMP1 for 30 min, AMP2 for 30 min, AMP3 for 15 min, channel-specific HRP reagent for 15 min, diluted TSA Plus fluorophores (PerkinElmer,USA) in RNAscope TSA dilution buffer (1:1000 dilution) for 30 min, HRP-blocker reagent for 15 min. Stained section was counterstained with DAPI solution and mounted in SlowFade Gold Antifade reagent (Invitrogen, S36936).

For dual RNA-FISH and immunostaining, tissue sections were pre-treated, and signals developed as described above. Following RNA-FISH, the sections were blocked with 10% normal goat serum/1%BSA in PBS, incubated with anti-RFP (1:50, Rockland, 600-401-379) or anti-cTnl (1:50, Abcam, ab47003) at 4°C overnight, HRP-conjugated secondary antibodies against rabbit (1:200, Invitrogen, #31470) for 30 min, diluted TSA Plus TMR (1:300, PerkinElmer, FP1169) in RNAscope TSA buffer for 15 min, and counterstained with DAPI.

Insoluble collagen assay—Insoluble collagen assay was conducted using Sircol Insoluble Collagen Assay Kit (Biocolor, S2000). The injured regions of the heart were harvested at 4 weeks following injury and weight their wet weight. Tissues were homogenized in 0.1 mg/ml pepsin/0.5M acetic acid and incubated overnight at 4°C. lysates were centrifuged at 12K r.p.m for 10min and supernatants were transfer to new tubes. Tissue residues were incubated with Fragmentation Reagent at 65°C for 2 h with vortex every 30 min during incubation, centrifuged at 12K r.p.m for 10 min, and supernatants were transferred into new tubes. Supernatants were mixed with 1ml of Sircol Dye Reagent and incubated for 30 min with gentle shaking. Precipitates were collected by centrifuge at 12K r.p.m for 10 min and washed with 750μl of ice-cold Acid-Salt Wash Reagent. Washed precipitates were dissolved in 500μl of Alkali Reagent, transferred 200μl of each sample and collagen standards into a 96-well plate, and measured absorbance at 550nm using Synergy H1 microplate reader (BioTeK).

Transmission electron microscopy—Samples were fixed in 2% glutaraldehyde in PBS at 4oC for 3 hour. Fixed samples were embedded in low-viscosity resin (Agar, UK) as following: samples were osmicated using 1% OsO4; stained with 3% uranyl-acetate; dehydrated in 30-50-70-95-100% ethanol and embedded in low-viscosity resin (Agar, UK). Plastic-embedded samples were sectioned using UCT ultramicrotome (Leica, Austria) and diamond knife (Diatome, Austria). Sections 50-55nm thick were mounted on home-made

EM grid(s) with plastic-carbon support film, stained with saturated uranyl-acetate and Sato's lead-citrate. Sections were imaged using JEM1200EX transmission electron microscope (JEOL, Japan) at 80 kV equipped with BioScan600W digital camera (Gatan, USA). Images were prepared for publication using a Photoshop (Adobe, USA). Approximately 500 fibrils were measured by ImageJ for analyzing fibril diameter in each group.

Tomography of collagen fibers—Sections 200 nm thick were mounted on 150 mesh hexagonal copper grids (Ted Pella, USA). Thereafter, grids with attached sections were stained with saturated uranyl acetate, lead citrate, 10nm gold from both sides. Layer of carbon was evaporated on top of the section. Grids were loaded into high-resolution tomography holder Model 2020 (Fischione, USA) and imaged with TF20 TEM (FEI, Netherlands) at 200 kV. To collect tomograms, FEI Batch Tomography software was used. The tomograms were processed using IMOD software (Kremer et al., 1996). Alignment of the stack was performed using fiducial markers (10 nm gold) on both sides of the tomogram. The final 3d model calculation was performed by SIRT (IMOD). Obtained 3d models were visualized in Chimera(Pettersen et al., 2004). They were filtered with Gaussian filter and segmented in Segger, part of Chimera package. Final models were imaged in Chimera also.

Plasmid construction and Lentivirus preparation—pLenti-Largen T antigen (Cat#18922), Lenti-pHIV-eGFP (Cat#21373), PSPAX2 (Cat#12260), PMD.G2 (Cat#12259), pLV-eGFP-Cre (Cat#86805) were purchased from Addgene. Total 13ug pasmids (object gene, PSPAX2, PMD.G2) was co-transfected into 75cm^2 flask with 293T cells in 10 ml DMEM Medium, 6-7ml fresh DMEM medium were changed after plasmids co-transfected 8-10 h. The medium was collected and centrifuged at 4°C in 500x g for 10 min after transfected 72 h. The medium with virus was aliquoted and stored at −80°C.

Isolation of primary culture adult cardiac fibroblast—5-7 hearts were harvested from wild-type C57Bl/6 mice or Col5a1 floxed mice. Valves and atriums were removed from the hearts, and the hearts rinsed in ice-cold HBSS. The hearts were chopped into 1mm square pieces, suspended in 0.1μg/ml liberase TH (Sigma, 5401151001) in Tyrodes buffer (136mM NaCl, 5.4mM KCl, 0.33mM NaH_2PO_4, 1mM $MgCl_2$, 10mM HEPES, 0.18% Glucose), and incubated with shaking incubator at 37°C for 30 min at 80 rpm. Digested hearts were filtered with a 40μm cell strainer (Fisher, 22363547), centrifuged at 200x g for 5 min, resuspended cells with 10ml of 20%FBS in F12K medium, and seeded the cells into 100mm^2 dish. After 2 h, medium was changed to human basic FGF (10ng/ml, Millipore, GF003) containing 20%FBS in F12K medium. Isolated cardiac fibroblast was used for experiments in 2nd or 3rd passage.

Generation of Col5a1 deficient immortalized cardiac fibroblast—Cardiac fibroblasts were isolated from Col5a1 fl/fl mouse as described above. These cells were infected with Lentivirus-Large T antigen in presence of polybrene (8μg/ml) for 16 h, treated with puromycin (2μg/ml) for selection of infected cells. Immortalized cells were cultured with 10%FBS containing high glucose DMEM. Cells so immortalized were then infected with Lentivirus-Cre recombinase or lentivirus-GFP to generate Col5a1 deficient cardiac fibroblast or control cardiac fibroblast, respectively. These cells were cultured for 6-7 days

and used for each experiment to determine effects on gene expression. To determine an effect of Cilengitide on these cells, Col5a1fl/fl cardiac fibroblasts were pretreated with Cilengitide (1μM) in 10%FBS containing high glucose DMEM for 1 h before infection with lentivirus-Cre recombinase or lentivirus-GFP. These cells were treated with Cilengitide/vehicle for 7 days and medium was changed every 2 days.

Flow cytometry—For cultured cardiac fibroblasts, cells were harvested and fixed in 4% formaldehyde/PBS for 10min on ice, incubated for primary antibodies diluted in 1%BSA/PBS for 1h on ice. For unconjugated antibodies, cells were incubated with diluted Alex Fluor 594 secondary antibody (1:200, Invitrogen). Data was analyzed using Flowjo software.

Measurement of force generated by Col V deficient cardiac fibroblasts.

Device fabrication: The device to make microtissues was designed using AutoCAD software (Autodesk Inc., USA). STAR Methods **Figure 1a** shows the three-dimensional (3D) design of master mold. STAR Methods **Figure 1b** shows the 3D schematic of the replicated design with wells and two microposts. The top view of the replicated design is shown in STAR Methods **Figure 1c**. By using a laser cutter with a fine-tuned laser power and speed, poly(methyl methacrylate) (PMMA) master molds were fabricated as shown in STAR Methods **Figure 1d**. After sticking the mold to a Petri dish with glue, a mixture of polydimethylsiloxane (PDMS) prepolymer and its curing agent with the mass ratio of 20:1 was prepared and poured on the mold. After removing bubbles and curing at 80 °C for 2 hours, the PDMS was peeled off from the mold as shown in STAR Methods **Figure 1e**.

Fabrication of microtissues: In order to make microtissues, after sterilizing the PDMS platform, a collagen hydrogel at density of 3 mg/ml was prepared. Cardiac fibroblasts were mixed with the gel at density of 5 Million cells/ml. The small well around microposts was filled with the cell-laden gel and then incubated for 1 hour to encourage the gel formation. After the incubation, sufficient cell culture media was added to the samples.

Measurement of contraction force of microtissues: The pictures of tissues were taken on days 1, 2, and 3 of culture by using ToupView microscope integrated with SeBaView software. The images were then analyzed with ImageJ software to measure the deflection of microposts due to the tissue contraction. The cantilever beam theory was used to quantify tissue force. This theory correlates the tissue force to small deflection of microposts as shown in STAR Methods **Figure 1f**.

The stiffness of microposts can be calculated by equation (1) and the contraction force can be calculated by equation (2) by measuring the deflection of the free end of each micropost as follows:

$$k = \frac{3\pi E d^4}{64 L^3}$$

$$F = k\delta$$

where k is the stiffness of each micropost that is a function of length (L), diameter (d), and Young's modulus of PDMS post (E). The Young's modulus of PDMS was considered to be 1.1 MPa (Brown et al., 2005; Wang et al., 2014). In the equation (2), F is the contraction force, δ is the deflection of free end of the micropost (Beussman et al., 2016; Ma et al., 2018; Oyunbaatar et al., 2016; Ribeiro et al., 2016).

Numerical simulation: To confirm the measurements of PDMS deflection and contraction force, finite element analysis (FEA) implemented in COMSOL Multiphysics 5.3 software was used. The FEM model consisted of two cylindrical PDMS microposts with the post height of 3.1 mm and diameter of 0.8 mm inside a well. The microposts were fixed to the well and deemed as a cantilever beam. The PDMS assembly was modeled as linear elastic material with a uniform Young's modulus of 1.1 MPa. After setting appropriate boundary conditions and by applying a single force to the free end of the microposts, the displacement distribution of the microposts were determined as illustrated in STAR Methods **Figure 1g**. Moreover, the simulation showed a linear relationship between the applied force and micropost deflection, which is in agreement with the cantilever beam theory (STAR Methods **Figure 1h**).

Measurement of decorrelation rate of Col V deficient cardiac fibroblasts.—

Quantitative phase microscopy (QPM) was used to determine decorrelation rate as follows. Cardiac fibroblasts were isolated from Col5a1 floxed mice, immortalized and then treated with a Cre expressing or GFP lentivirus to generate Col5a1CKO or control fibroblasts. Cells were imaged every 5 min for 20 h at 20x with a SID-4 Bio (Phasics) camera to acquire QPM data via quadriwave lateral shearing interferometry(Bon et al., 2009). This was on an Axio-vision Observer Z1 (Zeiss) equipped 0.4 numerical aperture objective lens with illumination was provided by a 660 nm center wavelength collimated LED (Thorlabs). The Col5a1CKO fibroblasts and the control fibroblasts were imaged with enough spacing between cells to allow for automated particle tracking (Crocker and Grier, 1996; Zangle et al., 2013a) and cell or cell cluster segmentation (Otsu, 1979; Zangle et al., 2013b). Automated detection of cell division events were done by pattern matching (Zangle et al., 2014) of quantitative phase images. Using experimentally determined cell average specific refractive index, quantitative phase shifts is related to the dry biomass of cells (Barer, 1952; Davies and Wilkins, 1952). All image processing was performed using custom MATLAB (MathWorks) scripts.

QPM decorrelation rate via temporal autocorrelation: We quantified the rate of biomass redistribution by examining the similarity of the QPM data over time through an unbiased estimate of autocorrelation (Bendat and Piersol, 2013) of the phase shift signal. The temporal autocorrelation was normalized with respect to the number of data points used in each autocorrelation window, referenced to the end of the time shift window (t_0), and defined as:

$$C_{\phi\phi}(x,y,t_0,\tau)=\frac{w}{\left(w-\frac{\tau}{\Delta t}\right)}\cdot\frac{\sum_{i=0}^{w-\tau/\Delta t}\phi(x,y,t_0-i\Delta t)\cdot\phi(x,y,t_0-i\Delta t-\tau)}{\sum_{i=0}^{w}\left[\phi(x,y,t_0-i\Delta t)\right]^2} \quad (1)$$

Where x and y are the spatial positions after removing rigid translational motion of the cell cluster, t_0 is the time, ϕ is phase shift, w is the number of images used to calculate the signal, and τ is time lag. The autocorrelation was then averaged over the cell or cluster area as:

$$\overline{C_{\phi\phi}(t_0,\tau)}=\frac{1}{A}\sum_{\text{all } x,y \text{ in } A} C_{\phi\phi}(x,y,t_0,\tau) \quad (2)$$

where A is the area of the cell or cluster in pixels. The slope of a linear least-squares fit to the averaged autocorrelation from $\tau = 0$ to $\tau = 1$ h (12 frames) was defined as the decorrelation rate and used to quantify the biomass redistribution rate within cell clusters. Any decorrelation rate measurements that included images with mitotic cells were excluded.

Traction force measurement of neonatal rat ventricle myocyte and fibroblast co-culture.

Fabrication of bio-sensor devices: The bio-sensor devices were fabricated by first spin coating a layer of photoresist (AZ 4620, 2500rpm, 60s) onto a glass slide, and baking it at 90 Celsius for 3 minutes. Then, gold nanoparticles suspended in citrate buffer (Sigma-Alrich 742090) were deposited onto the photoresist and left to dry in a vacuum desiccator (Thermo Scientific™ 53100250) overnight, as illustrated in STAR Methods **Figure 2a**. A mixture of polydimethylsiloxane (PDMS) comprising 1 part of Sylgard 184 (Dow Corning) with 6 parts of Sylgard 527 (Dow Corning) was then poured onto the surface of dried gold nanoparticles. The Sylgard mixture was put under vacuum to remove the air bubbles before a coverslip glass was put on top of it, as shown in STAR Methods Figure 2b. The devices were then left to cure in the oven at 60 Celsius for 12 hours. Thereafter, the devices were released by immersing them into acetone overnight to dissolve the photoresist. This reveals the final structure shown in STAR Methods **Figure 2c**.

Cell Seeding and Microscopy: Matrigel (at concentration of 83μg/mL) was then coated for 12 hours on the surface of the PDMS devices. On day 1, neonatal rat ventricular cardiomyocytes (NRVMs) were seeded at 75% confluence on the devices for the mutant group, and at 90% confluence on the devices for the control group. The confluence in the 2 groups was made different in order to account for the fact that each mutant fibroblast occupies 3 times more area than each control fibroblast. On day 2, control and mutant fibroblasts were separately seeded onto their respective devices. On day 3, the cells were stained with Calcein AM (Invitrogen™), before they were imaged under dark field and fluorescence microscopy (Zeiss AxioScope A1, EC Epiplan-Neofluar, 20x, N.A.=0.5). The gold nanoparticles were also imaged under dark field microscopy. The gold nanoparticles moved when the cells were beating, due to the mechanical coupling between the cells and the substrate.

Machine Learning Model: Before we could process the images obtained from microscopy, the numerical model needed to be built. The numerical model was built by first generating 1000 different random continuous stress distributions in COMSOL (finite element software) by using 2-dimensional random functions. An example of the stress distribution is shown in STAR Methods **Figure 2d**. The stress distributions were applied as boundary loads onto the top surface of the device in COMSOL. Stationary studies were done in COMSOL to solve for the equilibrium displacement of the PDMS surface. One example of the displacement of the PDMS surface is shown in STAR Methods **Figure 2e**. Thereafter, the 1000 different cases of stresses and displacements were used to train the linear regression machine learning model (scikit-learn).

Processing of Experimental Images: An area spanning 200μm by 200μm was selected from the video taken by a 20x magnification objective lens under a dark field microscope (Zeiss AxioScope A1, EC Epiplan-Neofluar, 20x, N.A.=0.5). Two image frames were used to calculate the displacement of the gold nanoparticles. The reference frame was chosen as the frame in which the cells were not beating. The peak frame was chosen as the frame in which the cells and gold nanoparticles had the largest displacement. The positions of the gold nanoparticles were determined using the Gaussian fitting method as described(Xiao et al., 2018). The displacement was taken to be the difference in the positions of the gold nanoparticles between the peak frame and the reference frame. STAR Methods **Figure 2f,g** show the displacement of each of the gold nanoparticles. The displacements in STAR Methods **Figure 2f,g** were then interpolated and a two-dimensional Fourier transform filter was applied to process the interpolated data to eliminate the components of high spatial frequencies. The resulting interpolated displacements after Fourier filtering are shown in STAR Methods **Figure 2h,i**. The displacements from STAR Methods **Figure 2h,i** were then input into the machine learning model. The machine learning model then output the stress distributions as shown in STAR Methods **Figure 2j,k**. The predicted stress distributions were then inputted back into the COMSOL software to confirm that the simulated displacements (STAR Methods **Figure 2l**) match with the interpolated displacements (STAR Methods **Figure 2h**) with an overall error of 2% for the control group. The overall error of the displacements was 10% for the mutant group (STAR Methods **Figure 2i,m)**. The errors were calculated by the expression:

$$\sigma = \frac{\Sigma_{x,y}\left(u_{simulated}(x,y) - u_{actual}(x,y)\right)^2 + \Sigma_{x,y}\left(v_{simulated}(x,y) - v_{actual}(x,y)\right)^2}{\Sigma_{x,y}\left(u_{actual}(x,y)\right)^2 + \Sigma_{x,y}\left(v_{actual}(x,y)\right)^2}$$

where $u_{simulated}(x, y)$ and $v_{simulated}(x, y)$ are the x and y vector components of the simulated displacement from COMSOL in STAR Methods **Figure 2l**, and $u_{actual}(x, y)$ and $v_{actual}(x, y)$ are the x and y vector components of the displacement in STAR Methods **Figure 2h**. Note that the displacements are functions over space (x,y). It can be seen that the magnitude of the stresses is larger for the control group STAR Methods **Figure 2j** as compared to the mutant group STAR Methods **Figure 2k**.

Parallel microfiltration—To measure the deformability of wild-type and *Col5a1* null fibroblasts, we used parallel microfiltration (PMF) as described in our previous studies(Kim et al., 2016; Kim et al., 2019; Qi et al., 2015) to assess the ability of cells in a suspended state to filter through 10 μm pores of a membrane in response to applied pressure. The volume of retained cell suspension retained in the top well indicates the number of pores that are occluded, which is largely determined by cell deformability: lower retention indicates a sample with more deformable cells. Polycarbonate membranes with 10 μm pore size (TCTP14250, Millipore) were used for all filtration experiments. Prior to the PMF assay, trypsinized cells were rested 20 m at room temperature, counted using an automated cell counter (TC20, Bio-Rad), and resuspended in medium to a density of 5×10^5 cells/mL. Cell suspensions (400 μL) were loaded into each well of a 96-well plate sample loading plate (4 wells per sample). We measured cell viability by staining cells with Trypan Blue (T8154, Sigma) and verified that cell suspensions prior to filtration consisted of single cells; therefore, the filtration behavior is largely determined by the occlusion of viable single cells rather than apoptotic cells or larger aggregates of cells. Since cell size can also impact occlusion, we measured cell size distributions and confirmed there were no significant size differences between wild-type and knock-out cells in a suspended state (Fig S7A). To drive cell suspensions to filter through the 10 μm pores, we applied an air pressure of 2.0 kPa for 30 s. To quantify retention volume, we transferred the cell suspension retained in the top well after filtration to a 96-well plate and measured the absorbance of phenol red at 562 nm using a plate reader (SpectraMax M2, Molecular Devices). Using a standard curve, we calculated the retained volume. Retention was determined by the volume of cell suspension that remains in the top well after filtration divided by the initial volume loaded ($Volume_{final}$/$Volume_{initial}$).

Atomic force microscopy—For atomic force microscopy (AFM) experiments, PBS-perfused hearts were dissected and mounted in OCT (Tissue-Tek, Sakura Finetek, Torrance, CA, USA) and flash frozen in liquid nitrogen-cooled isopentane. Cardiac tissue cryosections (30 μm) were mounted onto microscope slides with an adhesive coating (#SUMGP14 Matsunami Glass Ind. Ltd., Kishiwada, Osaka, Japan). Cardiac sections were incubated in rabbit anti-mouse collagen type I antibody (CL50151AP-1; 1:250; Cedarlane Labs) in PBS at 4°C overnight and were detected by indirect immunofluorescence using Alexa Fluor 488 goat anti-rabbit secondary antibody (AB150156; 1:500; Abcam). AFM measurements were performed on each section in PBS using a JPK Nanowizard 4A BioAFM with a 200x200x200 μm HybridStage (Bruker/JPK BioAFM, Billerica, MA, USA) coupled to a Leica M205 stereoscope (Leica Microsystems, Wetzlar, Germany). Scar regions were identified by collagen I dense immunofluorescence signal which was used as a guide for overlaying the AFM cantilever for force spectroscopy (Figure 6B,C). Non-scar regions were selected in areas where collagen I signal was confined to the interstitial matrix surrounding cardiomyocytes and at least 1000 μm away from a scar region. Both scar regions and non-scar regions were probed with AppNano SHOCONGG-TL cantilevers with a 10 μm silicon dioxide sphere (nominal freq (kHz)= 21(8-38), k(N/m)= 0.14 (0.01-0.6); AppNano, Mountain View, CA, USA). The sensitivity and spring constant of each probe were calibrated before each experiment using the contact-free calibration method. All measurements were taken in force spectroscopy mode and force-vs-indentation curves were

generated from an average of 200 points/sample. Approach and retraction speeds for all force measurements were 2 μm/sec with a setpoint force of 2.5 nN and a retraction distance of 10 μm. Data analysis was performed using JPKSPM Data Processing software. To evaluate tissue stiffness, Young's modulus was calculated from >100 AFM force curves, using the Hertz-Sneddon model (IN, 1965). Young's modulus data were plotted and statistics calculated in GraphPad (Prism) software using the Kolmogorov-Smirnov nonparametric test.

Quantification and Statistical Analysis

All data is presented as mean ± standard deviation (SD) except Figure 6D (mean ± SEM) and mentioned in the figure legends. The exact value of n is mentioned in the figure legends and always stands for separate biological replicates. Statistical analysis was performed using GraphPad (Prism) software using Student's t-test (Two tailed) and one-way ANOVA with Tukey's multiple comparison analysis as appropriate. A P value <0.05 was considered as statistically significant. For analysis of strain imaging data, outlier identification was conducted in ROUT (Q=2%) method using GraphPad (Prism) software. The values identified as outlier were excluded from statistical analysis.

Supplementary Material

Refer to Web version on PubMed Central for supplementary material.

Acknowledgements

We thank Dr. Eric Olson, University of Texas Southwestern Medical Center and Dr Andrew Leask, University of Western Ontario, Canada for providing us the TCF21MerCreMer and the Col1a2CreERT mice respectively. We thank Dr. Siobhan Braybrook (UCLA) for AFM expertise. This work was funded by NIH grants (HL129178, HL137241, AR075867, HL126204, HL147883), Department of Defense grants (W81XWH-17-1-0464, W81XWH-20-1-0238), National Science Foundation grant (BMMB-1906165), grants from the Eli and Edythe Broad Stem Cell Center at UCLA and California Nanosystems Institute (BSCRC/CNSI innovation award) and James Eason Cardiovascular Discovery Funds. This research was also partly supported by NIH National Center for Advancing Translational Science (NCATS) UCLA CTSI Grant Number UL1TR001881. J.L.M. was supported by UPLIFT: UCLA Postdocs' Longitudinal Investment in Faculty (NIH K12 GM106996).

References

Acharya A, Baek ST, Banfi S, Eskiocak B, and Tallquist MD (2011). Efficient inducible Cre-mediated recombination in Tcf21 cell lineages in the heart and kidney. Genesis 49, 870–877. [PubMed: 21432986]

Asano Y, Ihn H, Yamane K, Jinnin M, Mimura Y, and Tamaki K (2005). Increased expression of integrin alpha(v)beta3 contributes to the establishment of autocrine TGF-beta signaling in scleroderma fibroblasts. J Immunol 175, 7708–7718. [PubMed: 16301681]

Bagnato GL, Irrera N, Pizzino G, Santoro D, Roberts WN, Bagnato G, Pallio G, Vaccaro M, Squadrito F, Saitta A, et al. (2018). Dual alphavbeta3 and alphavbeta5 blockade attenuates fibrotic and vascular alterations in a murine model of systemic sclerosis. Clin Sci (Lond) 132, 231–242. [PubMed: 29237724]

Barer R (1952). Interference microscopy and mass determination. Nature 169, 366–367. [PubMed: 14919571]

Bashey RI, Martinez-Hernandez A, and Jimenez SA (1992). Isolation, characterization, and localization of cardiac collagen type VI. Associations with other extracellular matrix components. Circ Res 70, 1006–1017. [PubMed: 1568294]

Belvisi L, Riccioni T, Marcellini M, Vesci L, Chiarucci I, Efrati D, Potenza D, Scolastico C, Manzoni L, Lombardo K, et al. (2005). Biological and molecular properties of a new alpha(v)beta3/alpha(v)beta5 integrin antagonist. Mol Cancer Ther 4, 1670–1680. [PubMed: 16275988]

Bendat JS, and Piersol AG (2013). Random data : analysis and measurement procedures.

Beussman KM, Rodriguez ML, Leonard A, Taparia N, Thompson CR, and Sniadecki NJ (2016). Micropost arrays for measuring stem cell-derived cardiomyocyte contractility. Methods 94, 43–50. [PubMed: 26344757]

Bon P, Maucort G, Wattellier B, and Monneret S (2009). Quadriwave lateral shearing interferometry for quantitative phase microscopy of living cells. Opt Express 17, 13080–13094. [PubMed: 19654713]

Brown XQ, Ookawa K, and Wong JY (2005). Evaluation of polydimethylsiloxane scaffolds with physiologically-relevant elastic moduli: interplay of substrate mechanics and surface chemistry effects on vascular smooth muscle cell response. Biomaterials 26, 3123–3129. [PubMed: 15603807]

Crocker JC, and Grier DG (1996). Methods of digital video microscopy for colloidal studies. J Colloid Interf Sci 179, 298–310.

Davies HG, and Wilkins MH (1952). Interference microscopy and mass determination. Nature 169, 541. [PubMed: 14929230]

Deb A, Skelding KA, Wang S, Reeder M, Simper D, and Caplice NM (2004). Integrin profile and in vivo homing of human smooth muscle progenitor cells. Circulation 110, 2673–2677. [PubMed: 15313945]

Dechantsreiter MA, Planker E, Matha B, Lohof E, Holzemann G, Jonczyk A, Goodman SL, and Kessler H (1999). N-Methylated cyclic RGD peptides as highly active and selective alpha(V)beta(3) integrin antagonists. J Med Chem 42, 3033–3040. [PubMed: 10447947]

Dobin A, Davis CA, Schlesinger F, Drenkow J, Zaleski C, Jha S, Batut P, Chaisson M, and Gingeras TR (2013). STAR: ultrafast universal RNA-seq aligner. Bioinformatics 29, 15–21. [PubMed: 23104886]

Frangogiannis NG (2017). The extracellular matrix in myocardial injury, repair, and remodeling. J Clin Invest 127, 1600–1612. [PubMed: 28459429]

Frangogiannis NG (2019). The Extracellular Matrix in Ischemic and Nonischemic Heart Failure. Circ Res 125, 117–146. [PubMed: 31219741]

Ghali N, Sobey G, and Burrows N (2019). Ehlers-Danlos syndromes. Bmj 366, l4966. [PubMed: 31533917]

Ghazalpour A, Rau CD, Farber CR, Bennett BJ, Orozco LD, van Nas A, Pan C, Allayee H, Beaven SW, Civelek M, et al. (2012). Hybrid mouse diversity panel: a panel of inbred mouse strains suitable for analysis of complex genetic traits. Mamm Genome 23, 680–692. [PubMed: 22892838]

Gulati A, Jabbour A, Ismail TF, Guha K, Khwaja J, Raza S, Morarji K, Brown TD, Ismail NA, Dweck MR, et al. (2013). Association of fibrosis with mortality and sudden cardiac death in patients with nonischemic dilated cardiomyopathy. Jama 309, 896–908. [PubMed: 23462786]

Heras-Bautista CO, Mikhael N, Lam J, Shinde V, Katsen-Globa A, Dieluweit S, Molcanyi M, Uvarov V, Jutten P, Sahito RGA, et al. (2019). Cardiomyocytes facing fibrotic conditions re-express extracellular matrix transcripts. Acta Biomater 89, 180–192. [PubMed: 30862552]

Hinkel R, Ball HL, DiMaio JM, Shrivastava S, Thatcher JE, Singh AN, Sun X, Faskerti G, Olson EN, Kupatt C, et al. (2015). C-terminal variable AGES domain of Thymosin beta4: the molecule's primary contribution in support of post-ischemic cardiac function and repair. J Mol Cell Cardiol 87, 113–125. [PubMed: 26255251]

Hynes RO (2002). Integrins: bidirectional, allosteric signaling machines. Cell 110, 673–687. [PubMed: 12297042]

Ieda M, Tsuchihashi T, Ivey KN, Ross RS, Hong TT, Shaw RM, and Srivastava D (2009). Cardiac fibroblasts regulate myocardial proliferation through beta1 integrin signaling. Dev Cell 16, 233–244. [PubMed: 19217425]

IN S (1965). The relation between load and penetration in the axis symmetric boussinesq problem for a punch of arbitrary profile. Int J Eng Sci 3, 47–57.

Kanisicak O, Khalil H, Ivey MJ, Karch J, Maliken BD, Correll RN, Brody MJ, SC JL, Aronow BJ, Tallquist MD, et al. (2016). Genetic lineage tracing defines myofibroblast origin and function in the injured heart. Nat Commun 7, 12260. [PubMed: 27447449]

Katsumi A, Orr AW, Tzima E, and Schwartz MA (2004). Integrins in mechanotransduction. J Biol Chem 279, 12001–12004. [PubMed: 14960578]

Kim TH, Gill NK, Nyberg KD, Nguyen AV, Hohlbauch SV, Geisse NA, Nowell CJ, Sloan EK, and Rowat AC (2016). Cancer cells become less deformable and more invasive with activation of beta-adrenergic signaling. J Cell Sci 129, 4563–4575. [PubMed: 27875276]

Kim TH, Ly C, Christodoulides A, Nowell CJ, Gunning PW, Sloan EK, and Rowat AC (2019). Stress hormone signaling through beta-adrenergic receptors regulates macrophage mechanotype and function. FASEB J 33, 3997–4006. [PubMed: 30509116]

Kremer JR, Mastronarde DN, and McIntosh JR (1996). Computer visualization of three dimensional image data using IMOD. Journal of structural biology 116, 71–76. [PubMed: 8742726]

Lincoln J, Florer JB, Deutsch GH, Wenstrup RJ, and Yutzey KE (2006). ColVa1 and ColXIa1 are required for myocardial morphogenesis and heart valve development. Dev Dyn 235, 3295–3305. [PubMed: 17029294]

Liu S, Xu SW, Blumbach K, Eastwood M, Denton CP, Eckes B, Krieg T, Abraham DJ, and Leask A (2010). Expression of integrin beta1 by fibroblasts is required for tissue repair in vivo. J Cell Sci 123, 3674–3682. [PubMed: 20940256]

Lusis AJ, Seldin MM, Allayee H, Bennett BJ, Civelek M, Davis RC, Eskin E, Farber CR, Hui S, Mehrabian M, et al. (2016). The Hybrid Mouse Diversity Panel: a resource for systems genetics analyses of metabolic and cardiovascular traits. J Lipid Res 57, 925–942. [PubMed: 27099397]

Lygoe KA, Norman JT, Marshall JF, and Lewis MP (2004). AlphaV integrins play an important role in myofibroblast differentiation. Wound Repair Regen 12, 461–470. [PubMed: 15260812]

Ma X, Dewan S, Liu J, Tang M, Miller KL, Yu C, Lawrence N, McCulloch AD, and Chen S (2018). 3D printed micro-scale force gauge arrays to improve human cardiac tissue maturation and enable high throughput drug testing. Acta Biomater.

Mali P, Ye Z, Hommond HH, Yu X, Lin J, Chen G, Zou J, and Cheng L (2008). Improved efficiency and pace of generating induced pluripotent stem cells from human adult and fetal fibroblasts. Stem Cells 26, 1998–2005. [PubMed: 18511599]

Otsu N (1979). Threshold Selection Method from Gray-Level Histograms. Ieee T Syst Man Cyb 9, 62–66.

Oyunbaatar NE, Lee DH, Patil SJ, Kim ES, and Lee DW (2016). Biomechanical Characterization of Cardiomyocyte Using PDMS Pillar with Microgrooves. Sensors (Basel) 16.

Pettersen EF, Goddard TD, Huang CC, Couch GS, Greenblatt DM, Meng EC, and Ferrin TE (2004). UCSF Chimera--a visualization system for exploratory research and analysis. J Comput Chem 25, 1605–1612. [PubMed: 15264254]

Pillai IC, Li S, Romay M, Lam L, Lu Y, Huang J, Dillard N, Zemanova M, Rubbi L, Wang Y, et al. (2017). Cardiac Fibroblasts Adopt Osteogenic Fates and Can Be Targeted to Attenuate Pathological Heart Calcification. Cell Stem Cell 20, 218–232 e215. [PubMed: 27867037]

Qi D, Kaur Gill N, Santiskulvong C, Sifuentes J, Dorigo O, Rao J, Taylor-Harding B, Ruprecht Wiedemeyer W, and Rowat AC (2015). Screening cell mechanotype by parallel microfiltration. Sci Rep 5, 17595. [PubMed: 26626154]

Rappsilber J, Mann M, and Ishihama Y (2007). Protocol for micro-purification, enrichment, pre-fractionation and storage of peptides for proteomics using StageTips. Nat Protoc 2, 1896–1906. [PubMed: 17703201]

Rau CD, Romay MC, Tuteryan M, Wang JJ, Santolini M, Ren S, Karma A, Weiss JN, Wang Y, and Lusis AJ (2017). Systems Genetics Approach Identifies Gene Pathways and Adamts2 as Drivers of Isoproterenol-Induced Cardiac Hypertrophy and Cardiomyopathy in Mice. Cell Syst 4, 121–128 e124. [PubMed: 27866946]

Rau CD, Wang J, Avetisyan R, Romay M, Martin L, Ren S, Wang Y, and Lusis AJ (2014). Mapping Genetic Contributions to Cardiac Pathology Induced by Beta-Adrenergic Stimulation in Mice. Circulation Cardiovascular genetics.

Ren J, Zhang S, Kovacs A, Wang Y, and Muslin AJ (2005). Role of p38alpha MAPK in cardiac apoptosis and remodeling after myocardial infarction. J Mol Cell Cardiol 38, 617–623. [PubMed: 15808838]

Ribeiro AJ, Denisin AK, Wilson RE, and Pruitt BL (2016). For whom the cells pull: Hydrogel and micropost devices for measuring traction forces. Methods 94, 51–64. [PubMed: 26265073]

Robinson MD, McCarthy DJ, and Smyth GK (2010). edgeR: a Bioconductor package for differential expression analysis of digital gene expression data. Bioinformatics 26, 139–140. [PubMed: 19910308]

Rog-Zielinska EA, Norris RA, Kohl P, and Markwald R (2016). The Living Scar--Cardiac Fibroblasts and the Injured Heart. Trends Mol Med 22, 99–114. [PubMed: 26776094]

Sarrazy V, Koehler A, Chow ML, Zimina E, Li CX, Kato H, Caldarone CA, and Hinz B (2014). Integrins alphavbeta5 and alphavbeta3 promote latent TGF-beta1 activation by human cardiac fibroblast contraction. Cardiovasc Res 102, 407–417. [PubMed: 24639195]

Scaringi C, Minniti G, Caporello P, and Enrici RM (2012). Integrin inhibitor cilengitide for the treatment of glioblastoma: a brief overview of current clinical results. Anticancer Res 32, 4213–4223. [PubMed: 23060541]

Sun M, Chen S, Adams SM, Florer JB, Liu H, Kao WW, Wenstrup RJ, and Birk DE (2011). Collagen V is a dominant regulator of collagen fibrillogenesis: dysfunctional regulation of structure and function in a corneal-stroma-specific Col5a1-null mouse model. J Cell Sci 124, 4096–4105. [PubMed: 22159420]

Truitt JM, Blednov YA, Benavidez JM, Black M, Ponomareva O, Law J, Merriman M, Horani S, Jameson K, Lasek AW, et al. (2016). Inhibition of IKKbeta Reduces Ethanol Consumption in C57BL/6J Mice. eNeuro 3.

Ubil E, Duan J, Pillai IC, Rosa-Garrido M, Wu Y, Bargiacchi F, Lu Y, Stanbouly S, Huang J, Rojas M, et al. (2014). Mesenchymal-endothelial transition contributes to cardiac neovascularization. Nature 514, 585–590. [PubMed: 25317562]

van den Borne SW, Diez J, Blankesteijn WM, Verjans J, Hofstra L, and Narula J (2010). Myocardial remodeling after infarction: the role of myofibroblasts. Nat Rev Cardiol 7, 30–37. [PubMed: 19949426]

Wang JJ, Rau C, Avetisyan R, Ren S, Romay MC, Stolin G, Gong KW, Wang Y, and Lusis AJ (2016). Genetic Dissection of Cardiac Remodeling in an Isoproterenol-Induced Heart Failure Mouse Model. PLoS genetics 12, e1006038. [PubMed: 27385019]

Wang Z, Volinsky AA, and Gallant ND (2014). Crosslinking effect on polydimethylsiloxane elastic modulus measured by custom-built compression instrument. Journal of Applied Polymer Science 131, n/a-n/a.

Weber KT (1989). Cardiac interstitium in health and disease: the fibrillar collagen network. J Am Coll Cardiol 13, 1637–1652. [PubMed: 2656824]

Welm BE, Dijkgraaf GJ, Bledau AS, Welm AL, and Werb Z (2008). Lentiviral transduction of mammary stem cells for analysis of gene function during development and cancer. Cell Stem Cell 2, 90–102. [PubMed: 18371425]

Wenstrup RJ, Florer JB, Brunskill EW, Bell SM, Chervoneva I, and Birk DE (2004). Type V collagen controls the initiation of collagen fibril assembly. J Biol Chem 279, 53331–53337. [PubMed: 15383546]

Wenstrup RJ, Florer JB, Willing MC, Giunta C, Steinmann B, Young F, Susic M, and Cole WG (2000). COL5A1 haploinsufficiency is a common molecular mechanism underlying the classical form of EDS. Am J Hum Genet 66, 1766–1776. [PubMed: 10777716]

Xiao F, Wen X, Tan XHM, and Chiou P-Y (2018). Plasmonic micropillars for precision cell force measurement across a large field-of-view. Applied Physics Letters 112, 033701. [PubMed: 29430022]

Zangle TA, Burnes D, Mathis C, Witte ON, and Teitell MA (2013a). Quantifying biomass changes of single CD8+ T cells during antigen specific cytotoxicity. PLoS One 8, e68916. [PubMed: 23935904]

Zangle TA, Chun J, Zhang J, Reed J, and Teitell MA (2013b). Quantification of Biomass and Cell Motion in Human Pluripotent Stem Cell Colonies. Biophys J 105, 593–601. [PubMed: 23931307]

Zangle TA, Teitell MA, and Reed J (2014). Live cell interferometry quantifies dynamics of biomass partitioning during cytokinesis. PLoS One 9, e115726. [PubMed: 25531652]

Zheng B, Zhang Z, Black CM, de Crombrugghe B, and Denton CP (2002). Ligand-dependent genetic recombination in fibroblasts : a potentially powerful technique for investigating gene function in fibrosis. Am J Pathol 160, 1609–1617. [PubMed: 12000713]

Zoppi N, Chiarelli N, Ritelli M, and Colombi M (2018). Multifaced Roles of the alphavbeta3 Integrin in Ehlers-Danlos and Arterial Tortuosity Syndromes' Dermal Fibroblasts. Int J Mol Sci 19.

Highlights

- Collagen V deficiency increases scar size after acute heart injury
- Mechanical properties of scars are altered with Col V deficiency
- Altered mechanosensitive cues augment myofibroblast formation in scar
- Inhibition of specific integrins rescues increased scarring in Col V deficient states

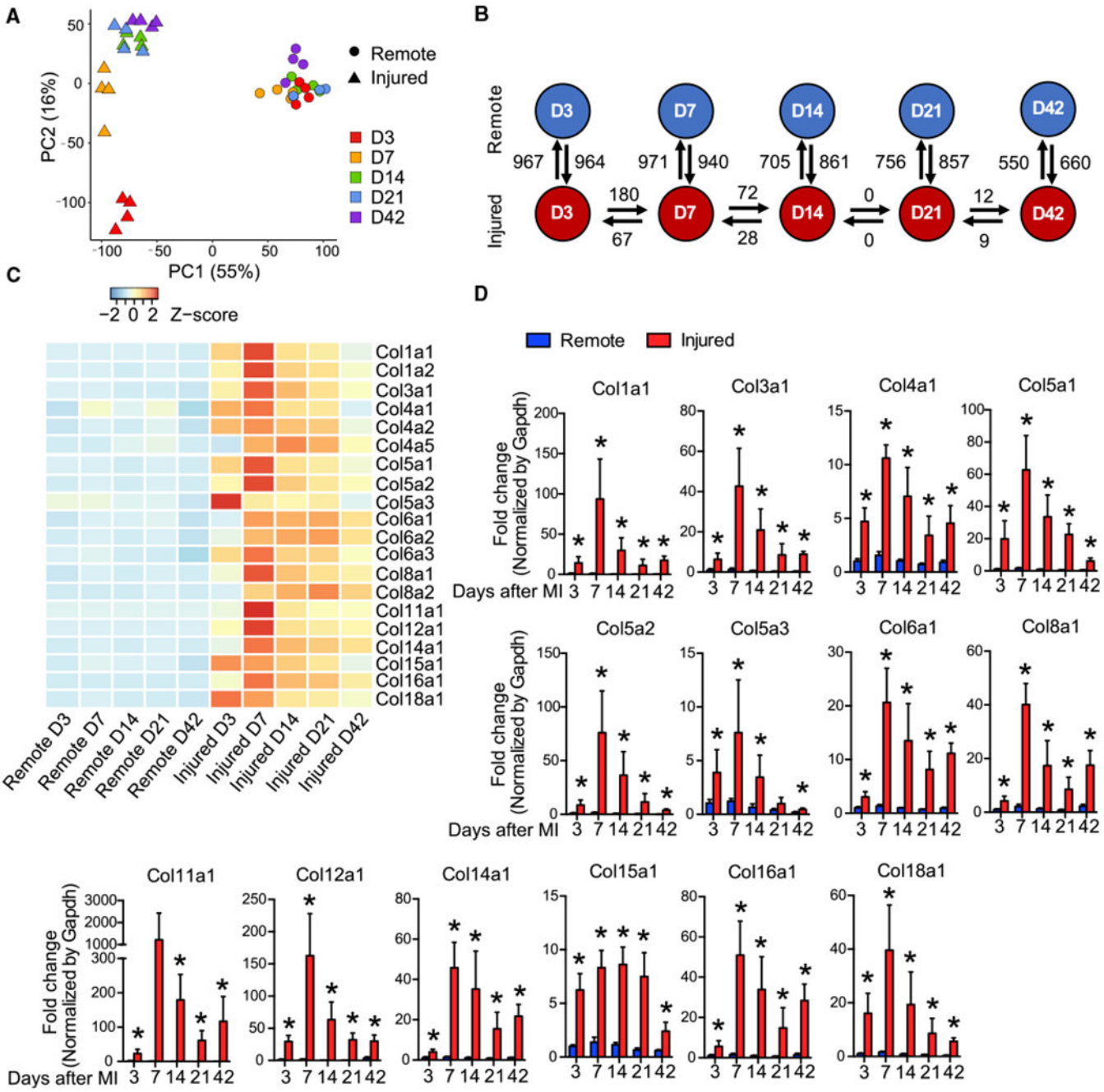

Fig 1. Temporal changes in gene expression of scar tissue following acute ischemic cardiac injury.

(A) Principal component analysis based on expression profiles of all genes (n=4) **(B)** Summary of differential gene expression analysis. Arrows and numbers indicate direction and numbers of differentially expressed genes detected in each pairwise comparison. (FDR 1%, fold change>4) **(C)** Heatmap with expression patterns of collagen genes (n=4). **(D)** Expression of collagen genes encoding for obligatory units of the respective collagen by qPCR (mean± S.D., *p<0.05, n=5)

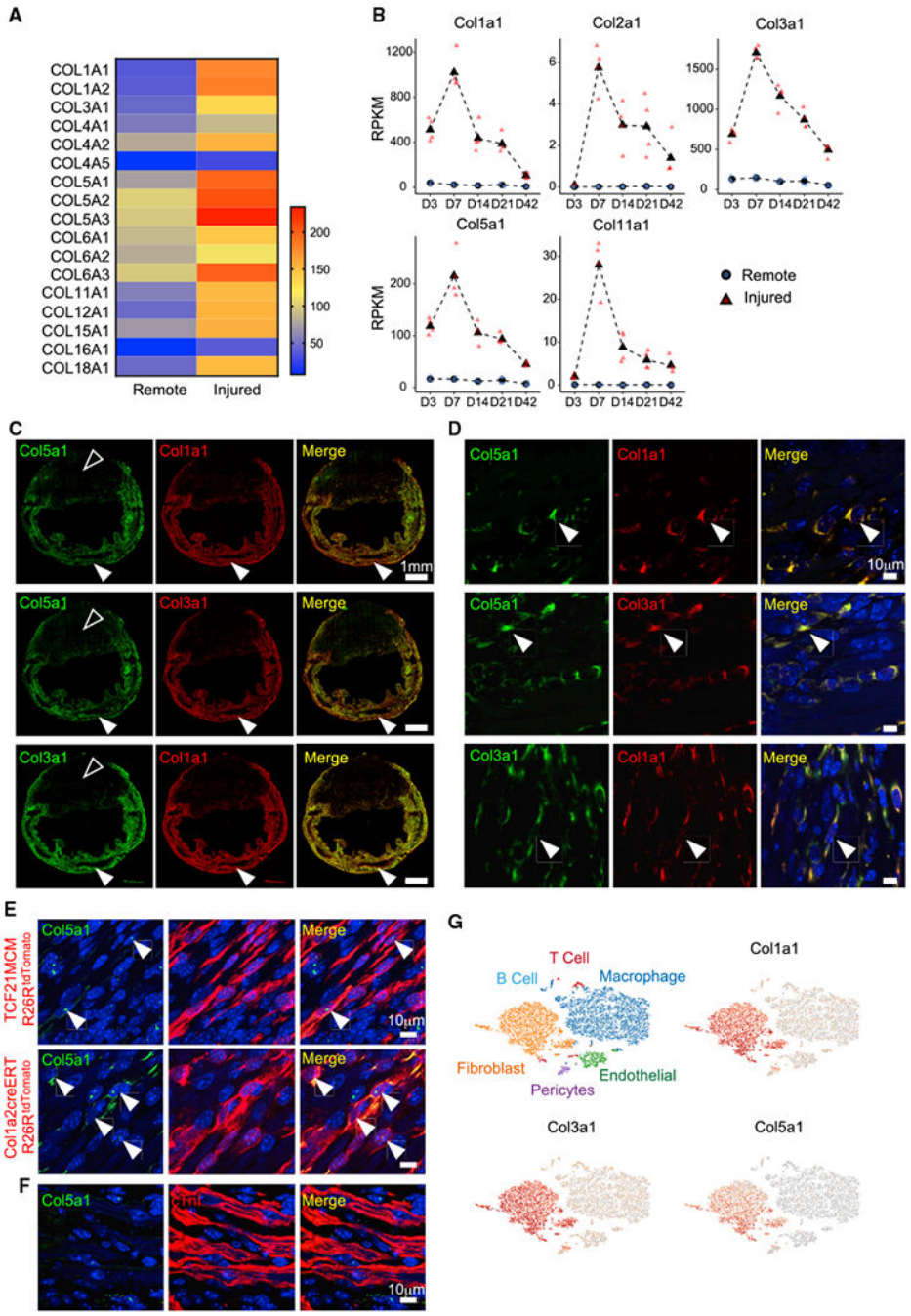

Figure 2. Expression of Col5a1 in relation to Col1a1 and Col3a1.

(A) Proteomic analysis of individual collagen chains in injured and remote region of myocardium at 7 days post MI (n=3). **(B)** Normalized expression levels (RPKM) for selected collagen genes. Average expression levels across timepoints are shown in black symbols and dashed lines. Expression levels for individual replicates are shown in colored symbols (n=4). **(C)** RNA-FISH to demonstrate expression of *Col5a1*, *Col1a1* and *Col3a1* in the heart at 7 days post-MI (solid arrowhead, representative images, n=4, unfilled arrowhead indicates remote region). **(D)** Higher magnification demonstrating co-localization of Col5a1

with Col1a1 and Col3a1 within the same cell (arrows, representative images, n=4). **(E)** Expression of *Col5a1* in cardiac fibroblasts genetically labeled by the TCF21 or Col1a2 label but **(F)** not in cardiomyocytes (Troponin I stained) in the injury region (arrows, representative images, n=3). **(G)** Single cell RNA-seq of non-myocytes at 7 days post-MI demonstrating typical cell phenotypes in clusters and distribution of *Col1a1*, *Col3a1* and *Col5a1* (n=3).

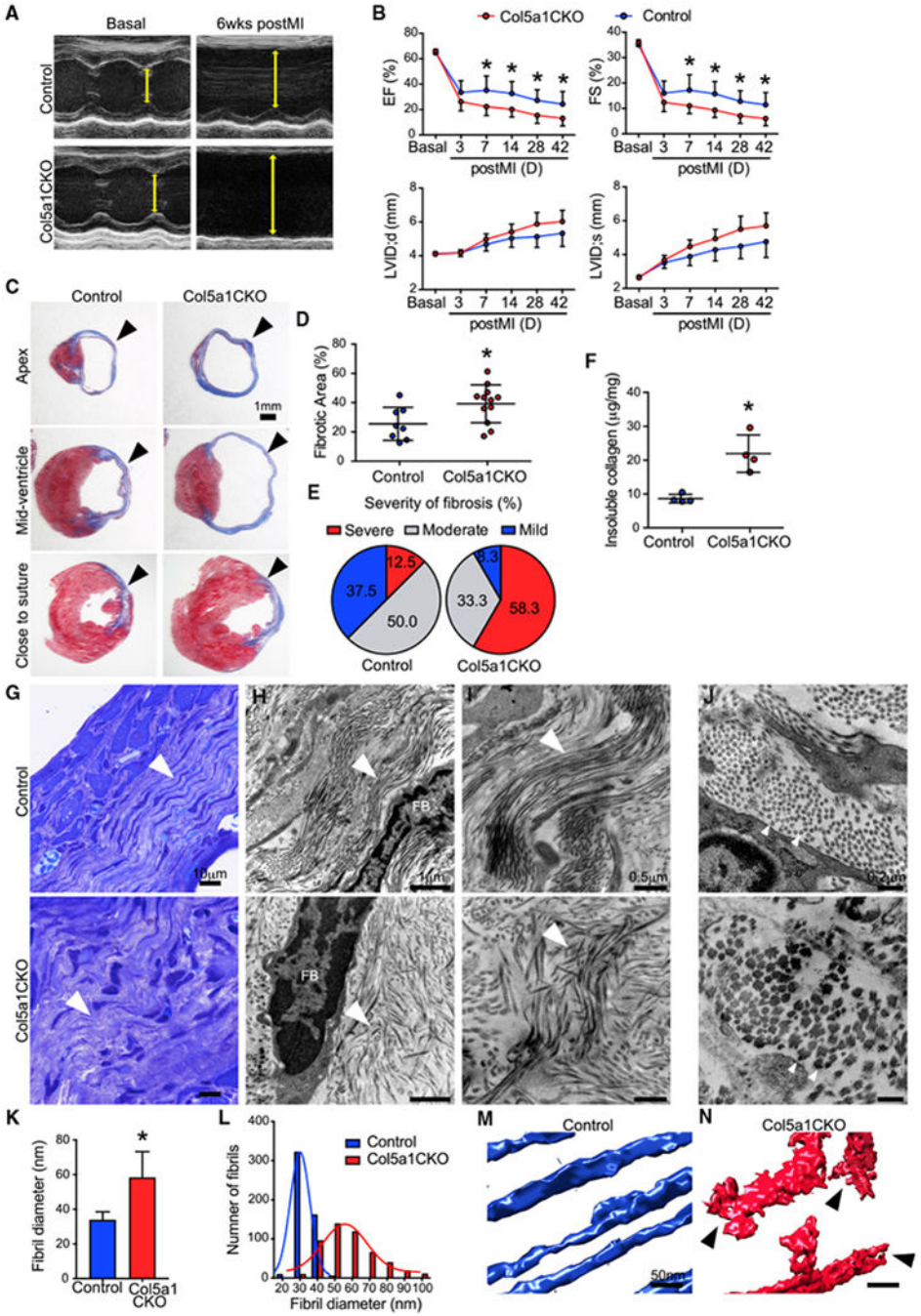

Figure 3. Animals with *Col5a1* deletion in cardiac fibroblasts exhibit a paradoxical increase in scar tissue after heart injury.

(A) M mode echocardiogram demonstrating left ventricular (LV) walls and internal dimension (yellow line) prior to basal and 6 weeks post-MI (representative images). **(B)** Ejection fraction (EF), Fractional shortening (FS), LV dimensions in end diastole (LVIDd) and end systole (LVIDs) at different time points post-MI (n=12/Control and 27/CKO at basal, n=10/Control and 22/CKO at 3D, n=9/Control and 15/CKO at 1wk, n=9/Control and 13/CKO at 2wks, n=8/Control and 12/CKO at 4 and 6wks post-MI) **(C)** Masson trichrome

staining of hearts sectioned at the base (just distal to suture line) at mid ventricle and apex 6 weeks post-MI (representative images) **(D)** Quantification of surface area of scar normalized to the surface area of the ventricle (n=8/Control and 12/CKO). **(E)** Fraction of animals demonstrating mild/moderate or severe scarring at 6 weeks post-MI. **(F)** Measurement of insoluble collagen in scar tissue at 4 weeks post-MI (n=4) **(G)** Toluidine blue staining of scar tissue at 4 weeks post-MI (arrowhead, representative images, n=2) **(H)** Transmission electron microscopy (TEM) of scar area showing fibrillar disarray in the Col5a1CKO (arrowhead, FB=fibroblast) **(I)** Higher magnification with TEM demonstrating fibrillar disarray with fibrils running in orthogonal axes to each other in the Col5a1CKO scar (arrowhead) **(J)** Cross sectional TEM view demonstrating fibril diameter size (arrowheads, n=2 for all TEM) **(K)** Average collagen fibril diameter in scars (n=2) **(L)** Histogram of collagen fibrils diameters demonstrates a clear shift to the right in Col5a1CKO (n=2) (**M, N)** Electron Tomogram of scar area from **(M)** Control and **(N)** Col5a1CKO animal. Data shown as mean± S.D., *p<0.05.

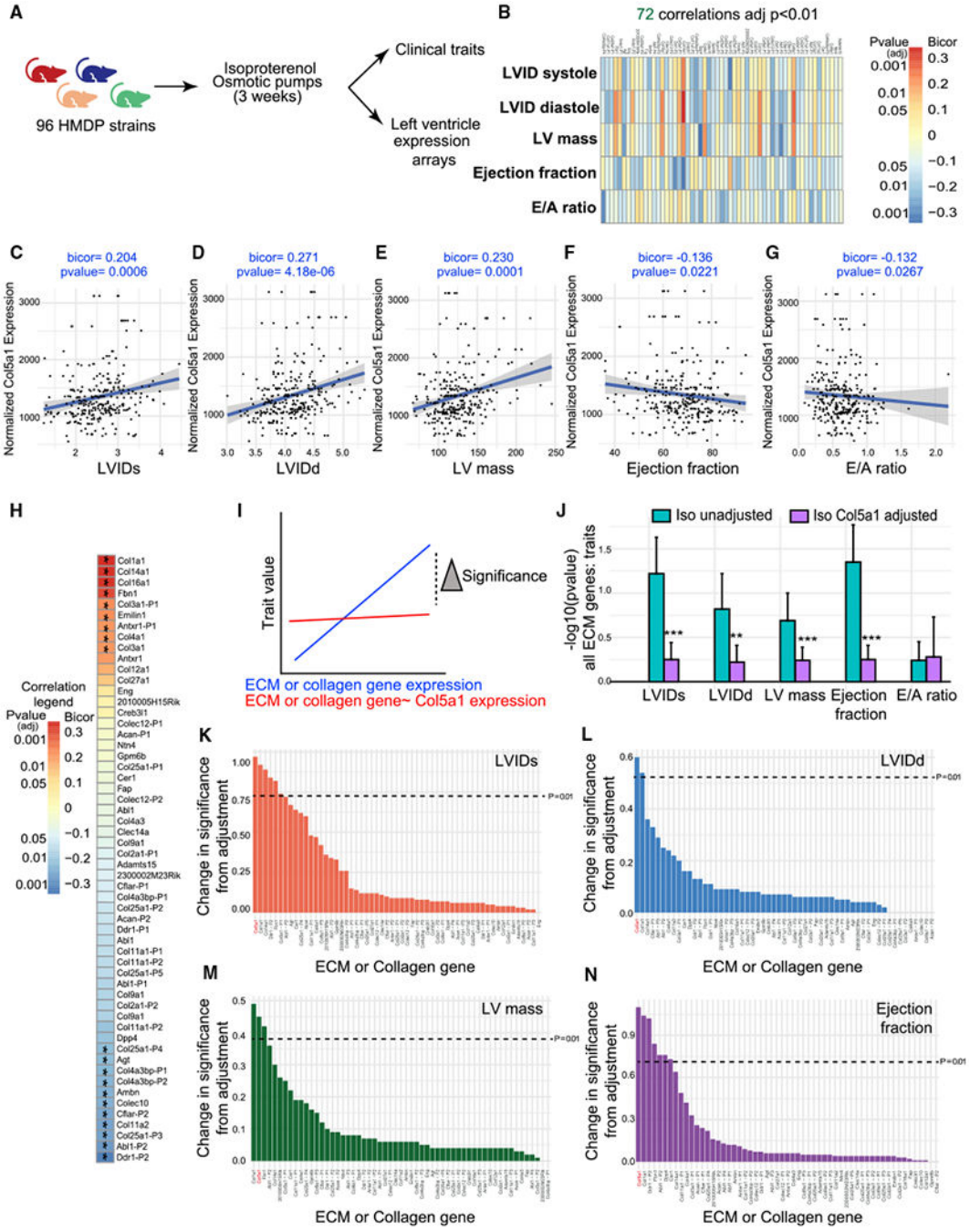

Fig 4. Importance of *Col5a1* in regulating cardiac function post injury vis-a-vis other ECM genes.

(A) HMDP comprising 96 strains of mice were subjected to continuous isoproterenol infusion for 3 weeks **(B)** Gene X trait analysis demonstrating strength of association between individual ECM genes and cardiac traits. (**C-G**) Scatter plots shows correlation of Col5a1 expression with traits of (**C**) LVIDs (**D**) LVIDd (**E**) LV mass (**F**) EF and (**G**) E/A ratio following isoproterenol injection across all HMDP strains. (**H**) Strength of association between Col5a1 expression and that of ECM genes (*p<0.01). **(I)** Hypothesis of how

adjustment for Col5a1 could significantly change the strength of association between ECM genes and cardiac traits **(J)** Conditional analysis demonstrating the strength of correlation (−log p value) between ECM genes and different cardiac traits following adjustment for Col5a1 expression (***p<0.005,**p<0.01, compared to isoproterenol unadjusted) **(K-N)** Change in significance of rest of ECM genes and specific trait **(K)** LVIDs **(L)** LVIDd **(M)** LV mass **(N)** EF following adjustment for specific gene (horizontal dotted line shows a cut off p value=0.01).

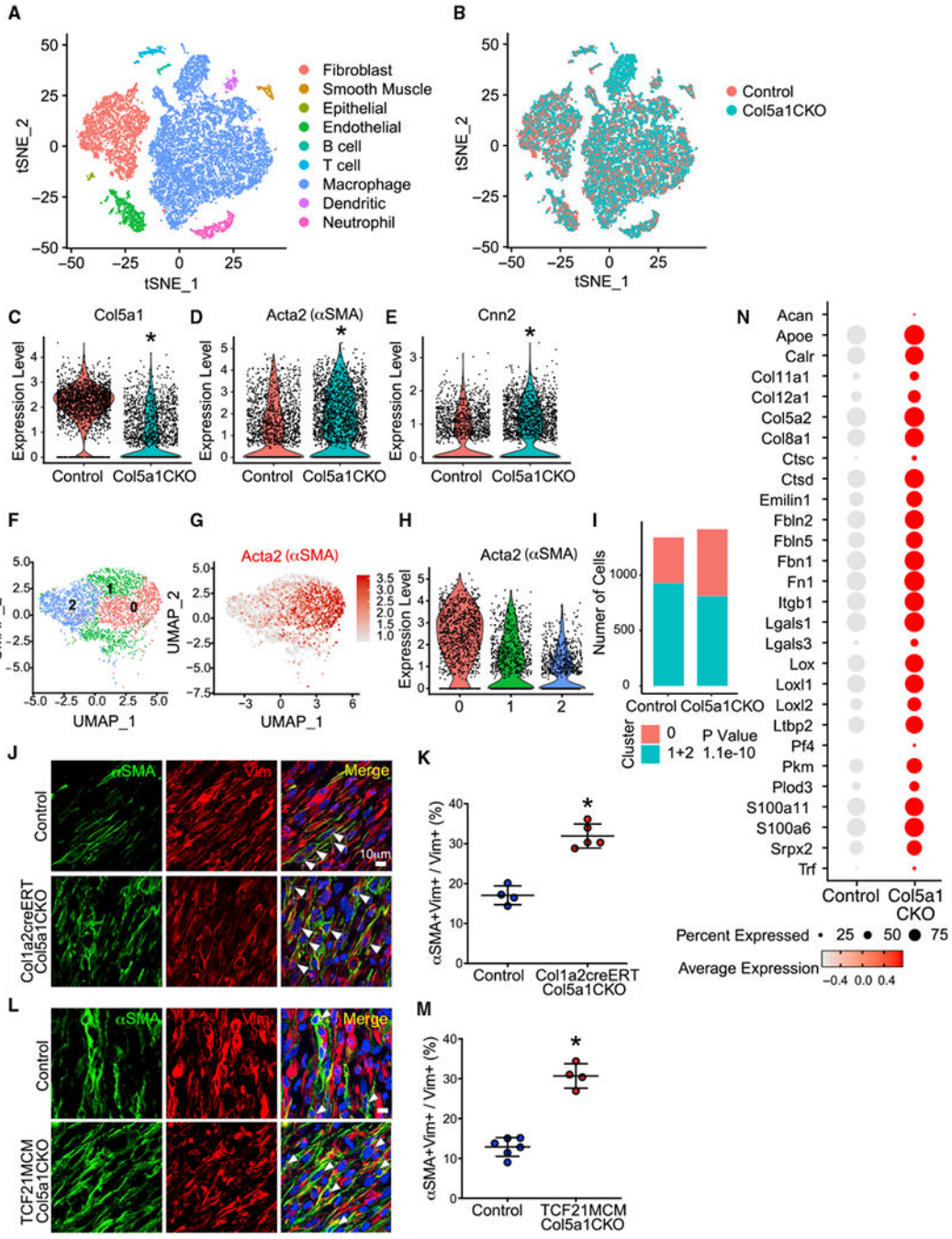

Fig 5. Single cell RNA-seq of non-myocytes of control and Col5a1CKO hearts harvested at 7 days following injury.

(A) tSNE plot demonstrating non-myocyte cell populations of the heart at 7 days post-MI **(B)** Distribution of non-myocyte cells from injured Control and Col5a1CKO hearts across these clusters. **(C-E)** Violin plot demonstrating expression of **(C)** Col5a1, **(D)** Acta2 (αSMA), **(E)** Cnn2 (Calponin) in fibroblast clusters. **(F)** Sub-clustering of fibroblast population **(G)** UMAP plot with expression of αSMA in fibroblast subclusters **(H)** Expression of Acta2 in subclusters of fibroblasts (**I**) Cell numbers in Cluster 0

(myofibroblasts) versus Cluster 1 and 2 (non-myofibroblasts) **(J)** Immunostaining for asmooth muscle actin (αSMA) and vimentin (Vim) in the scar of Col5a1CKO at 7 days post-MI (arrows, representative images) **(K)** Quantitation of the number of αSMA expressing myofibroblasts (n=4/Control and 5/CKO) **(L)** Immunostaining for αSMA and Vim in the scar of TCF21MCM:Col5a1CKO hearts at 7 days post-MI (arrows, representative images). **(M)** Quantitation of the number of αSMA expressing myofibroblasts (n=6/Control and 4/CKO) **(N)** Dot plot representing expression of ECM genes that are significantly upregulated in fibroblasts of Col5a1CKO hearts at 7 days post-MI (adjusted p value <0.05). Data shown as mean± S.D., *p<0.05.

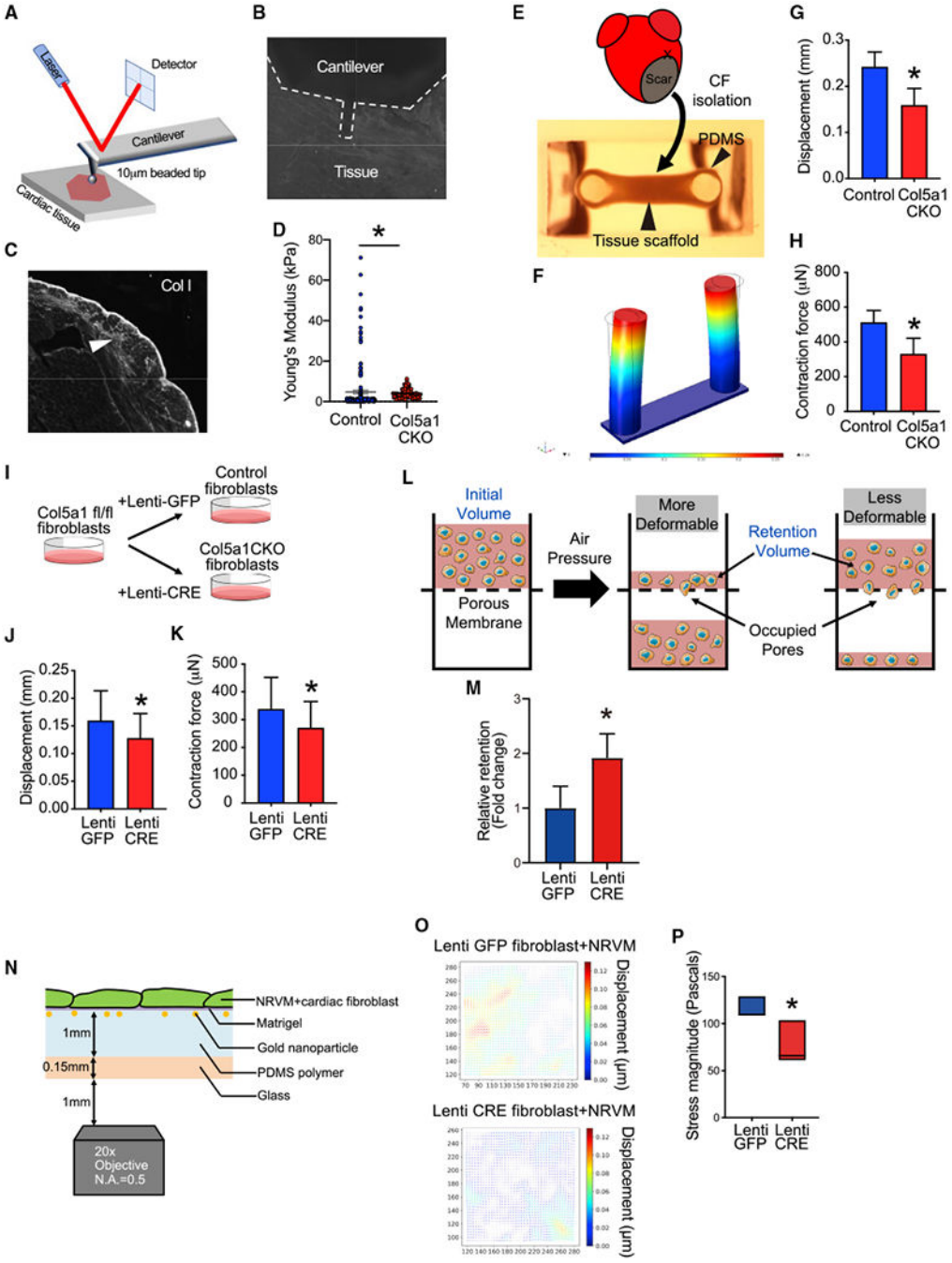

Fig 6. Col5a1CKO fibroblasts exhibit altered mechano-biological properties.

(A) Schematic illustration of atomic force microscopy (AFM) instrumentation **(B)** Representative image of AFM probe and cantilever over tissue section **(C)** Representative image of collagen I (Col I) indirect immunofluorescence detection in scar region (arrow) that was probed with AFM. **(D)** Young's Modulus measurements from injured regions (mean± SEM, *p<0.05, n=3). **(E-H)** Determination of mutant or control cardiac fibroblasts (CFs) to generate contractile forces. **(E)** CFs were isolated at 7 days post-MI and incorporated into hydrogel scaffolds and suspended between PDMS posts **(F)** Contraction of

CFs determined from displacement of PDMS posts. **(G)** Displacement of PDMS posts by CFs tissue scaffold (n=3) **(H)** Contraction forces generated by either Control or Col5a1CKO CFs (n=3) (**I-K**) Determination of contractile forces by generating Col5a1CKO CFs ex vivo. **(I)** CFs from hearts of Col5a1fl/fl mice were infected with a lentiviral Cre or GFP virus to create Col5a1 deficient CFs **(J)** Displacement of the PDMS posts and **(K)** contractile forces generated by Col5a1CKO CFs (n=3). (**L**) Schematic illustration of parallel microfiltration (PMF assay) **(M)** Relative retention of cells measured by PMF assay and normalized to the control (Lenti-GFP) CFs. (n=3) **(N)** Schematic of set up of Traction force microscopy where myocytes and CFs are seeded onto a matrigel layer containing gold labeled nanoparticles. **(O)** Heat maps demonstrating displacement of clusters of contracting myocytes and **(P)** determination of stress forces generated by myocytes in the presence of Col5a1CKO CFs (n=3). Data unless otherwise stated shown as mean± S.D., *$p<0.05$.

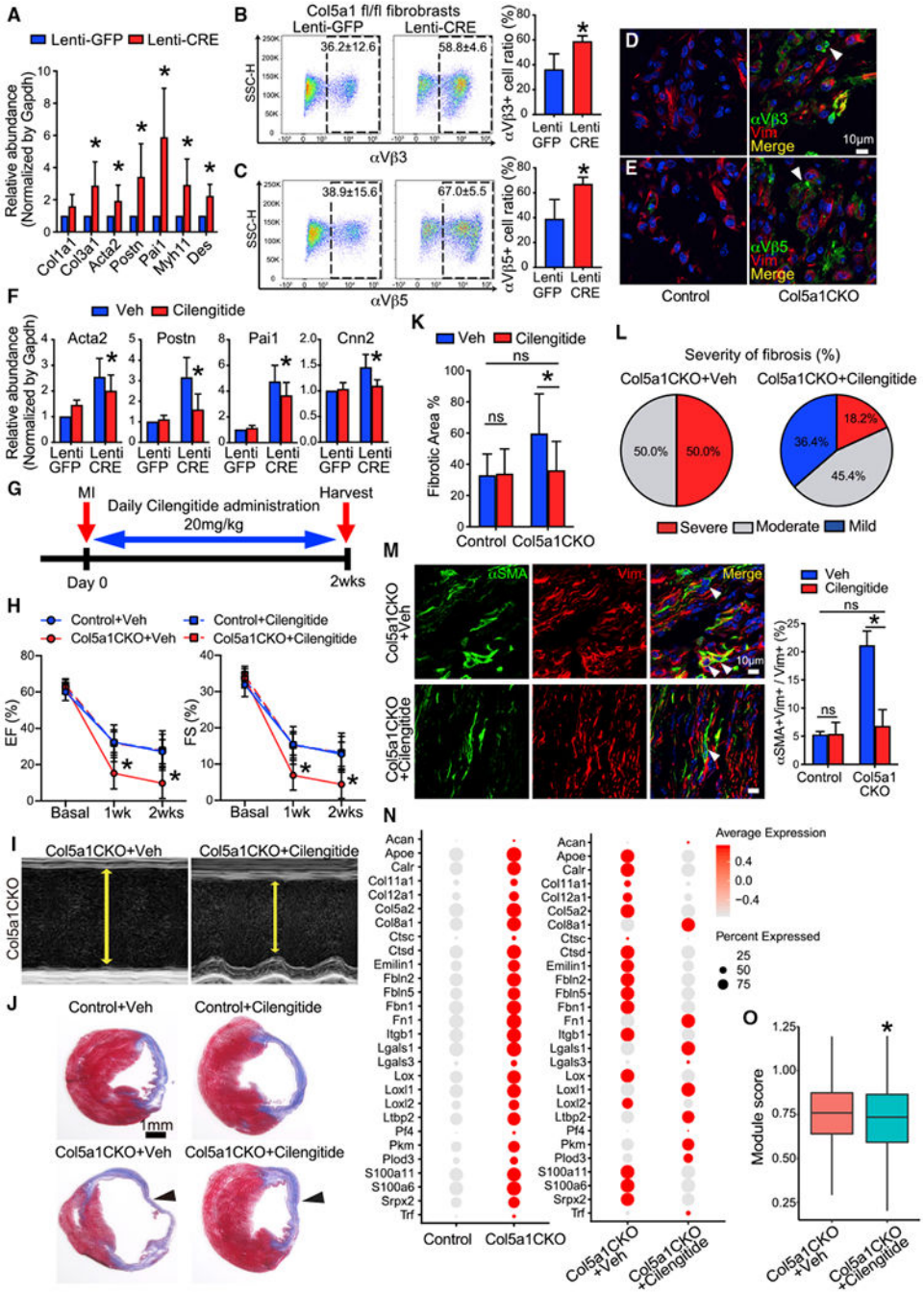

Fig 7. Inhibition of αvβ3 and αvβ5 integrins rescues increased scarring and cardiac dysfunction in Col5a1CKO animals.

(A) Expression of ECM and myofibroblast genes in Col5a1CKO CFs generated ex vivo (n=6) (**B,C**) Flow cytometry to determine expression of **(B)** αvβ3 and **(C)** αvβ5 integrins on Col5a1CKO CFs (n=6). **(D,E)** Immunostaining for Vim and **(D)** αvβ3, **(E)** αvβ5 in scar tissue at 7 days post-MI (arrows, representative images) **(F)** Expression of key myofibroblast genes in Col5a1CKO CFs in the presence or absence of cilengitide (n=6). **(G)** Experimental design to treat animals with daily cilengitide (20mg/kg) **(H)** EF/FS in control and

Col5a1CKO injected with cilengitide or vehicle (*Col5a1CKO+Cilengitide [red dotted line] vs. Col5a1CKO+Veh [red solid line], n=13/CKO+Cilengitide 10/other groups at basal, n=12/CKo+Cilengitide, 6/CKO+Veh, 9/Control+Cilengitide, 7/Control+Veh at 2wks post MI). (**I**) Representative images of M mode echocardiogram (yellow line indicates end systolic diameter) **(J)** Masson trichrome staining of mid ventricle at 2 weeks post-MI to show scar size (arrowhead, n=same number at 2 weeks post-MI as above) **(K)** Quantitation of fibrotic area (n=same number as above) **(L)** Fraction of Col5a1CKO animals demonstrating mild, moderate and severe fibrosis following PBS or cilengitide infusion **(M)** Immunostaining for αSMA and Vimentin in hearts of Col5a1CKO receiving PBS or cilengitide and quantitation of the fraction (arrows, representative images, n=10/CKO +Cilengitide, n=6/CKO+Veh, n=6/animals for all other groups). **(N)** Dot plot representing expression of ECM genes that are upregulated in CFs of Col5a1CKO hearts at 7 days post-MI compared to controls (left panel), the same genes were shown in fibroblasts from Col5a1CKO+Vehicle and Col5a1CKO+Cilengitide samples (right panel). **(O)** Box plot showing the module scores of 28 genes from (N) in fibroblasts from Col5a1CKO+Veh and Col5a1CKO+Cilengitide. Data shown as mean± S.D., *$p<0.05$, ns: Not significant.